広島大学学位論文

Spin filtered surface state scattering and electronic states of three-dimensional topological insulator Bi_2Te_2Se

（三次元トポロジカル絶縁体 Bi_2Te_2Se 表面の
スピン選択的電子散乱と電子構造）

2014 年

広島大学理学研究科
物理科学専攻

Munisai Nuermaimaiti

目次

Part Ⅰ　　主論文

Spin filtered surface state scattering and electronic states of three-dimensional topological insulator Bi_2Te_2Se

（三次元トポロジカル絶縁体 Bi_2Te_2Se 表面のスピン選択的電子散乱と電子構造）

Part II　　公表論文

(1) Unoccupied topological surface state in Bi_2Te_2Se.

Munisa Nurmamat, E. E. Krasovskii, K. Kuroda, M. Ye, K. Miyamoto, M. Nakatake, T. Okuda, H. Namatame, H. Namatame, M. Taniguchi, E. V. Chulkov, K. A. Kokh, O. E. Tereshchenko, A. Kimura.

Phys. Rev. B. **88**, 081301(R) (2013).

Part III　　参考論文

(1) Experimental verification of the surface termination in the topological insulator $TlBiSe_2$ using core-level photoelectron spectroscopy and scanning tunneling microscopy.

Kenta Kuroda, Mao Ye, Eike F. Schwier, **Munisa Nurmamat**, Kaito Shirai, Masashi Nakatake, Shigenori Ueda, Koji Miyamoto, Taichi Okuda, Hirofumi Namatame, Masaki Taniguchi, Yoshifumi Ueda, Akio Kimura.

Phys. Rev. B. **88**, 245308 (2013).

Part I

主論文

Doctoral thesis

Spin filtered surface state scattering and electronic states of three-dimensional topological insulator Bi_2Te_2Se

Munisa Nurmamat

****

Graduate School of Science

Hiroshima University

Higashi-Hiroshima

March 2014

List of Figures

2.1 Schematic picture of the tunneling junction and the energy level diagram for an elastic electron tunneling configuration 5

2.2 Schematic illustration of an experimental STM configuration 7

2.3 Schematic relationship of the energy level between tip and sample with different sample bias voltages 8

2.4 Generic STM operating modes 9

2.5 Schematic view of the photoemission process in the single-particle picture..... 12

3.1 Comparision of atomic insulator and two-dimensional quantum Hall state..... 20

3.2 Quantum Hall spin state and its band structure..... 23

3.3 Bulk band structure of HgTe/CdTe and their Experimental visualization of phase transition 24

3.4 Hexagonal warping effects and Oscillations on the surface of Bi_2Te_3 27

3.5 Prior studies on Bi_2Te_2Se 28

3.6 Comparison between the Dirac dispersion and the dispersion of a 2DEG with Rashba spin-orbit coupling 30

4.1 The LT-STM system in Hiroshima synchrotron radiation center 32

4.2 Chemical etching tool inset with tip procedure 35

4.3 Successfully etched tungsten tip 38

4.4 STM topography and dI/dV image on the clean surface of Si (111)..... 39

4.5 STS spectrum on the surface of Si (111)..... 41

4.6 Arrangement of experiment hall of Hisor and the schematic layout of the BL-7 in the top and side view 40

4.7 BL-7 experimental system 41

5.1 Crystal structure of Bi_2Te_2Se and the STM topographic images with several defects on the cleaved surface of Bi_2Te_2Se 45

5.2 Averaged STS spectrum and the energy-momentum ARPES intensity distribution map on the surface of Bi_2Te_2Se 47

5.3 Differential conductance map (dI/dV map) on the Bi_2Te_2Se surface at 4.5 K with various sample bias voltage 48

5.4 Fast Fourier transformed images for several bias voltages 50

5.5 FFT intensity profiles display the bias voltage dependent scattering and the ratio of the FFT intensity profiles along $\bar{\Gamma}\bar{M}$ and $\bar{\Gamma}\bar{K}$ directions 51

5.6 Fermi surface contours of the Bi_2Te_2Se surface state at different energies 52

5.7 The comparison of the FFT interference pattern with and without spin polarization calculated by $k.p$ theory and present work 53

5.8 Dispersion of scattering vectors from STM and $k.p$ theory inset show schematic and model constant energy contours 55

5.9 First principles electronic structure of a 7 formula units slab of Bi_2Te_2Se and the depth-momentum distribution of the charge density for TSS and ISS 56

5.10 Spatially resolved Fermi surfaces of Bi_2Te_2Se by *ab initio* calculation 58

5.11 Distribution of the spin polarization perpendicular to the surface of Bi_2Te_2Se by *ab initio* calculation 59

5.12 Visualized scattering vectors with schematic CEC and experimental FFT image and their dispersion 60

6.1 Depiction of interband optical excitation from bulk valence band to surface state before and after delay time 62

Contents

List of figures i

Contents iv

1 Introduction **1**

2 Theoretical Backgrounds **3**

2.1 The Scanning Tunneling Microscopy/Spectroscopy (STM/STS) 3

2.1.1 Tunneling current 3

2.1.2 Working principle of STM 7

2.1.3 Scanning tunneling spectroscopy (STS) 10

2.2 Angle-resolved photoemission spectroscopy (ARPES) 11

2.2.1 Photo electron spectroscopy (PES) 12

2.2.2 Angle-resolved photoemission spectroscopy 14

2.2.3 Synchrotron radiation 15

2.3 Electronic structure calculation 16

3 Topological insulators **18**

3.1 Topological phase of quantum matter 18

3.1.1 Quantum Hall effect (QHE) 19

3.1.2 Quantum spin Hall effect (QSHE) 22

3.2 Topological insulators in 2D 24

3.3 Topological surface state of 3D topological insulator 25

3.4 Backscattering in 3D topological insulators 29

4 Experimental techniques **32**

4.1 Description of the STM system 32

4.1.1 UHV system 33

4.1.2 Tip preparation 34

4.1.3 Tip anneling 36

4.1.4 Characterization of tips on Si (111) surface 37

4.2 ARPES setup 40

5 Direct observation of spin filtered surface state scattering in the Bi_2Te_2Se **43**

5.1 Electronic structure of Bi_2Te_2Se 43

5.1.1 Visualizing defects on the surface of Bi_2Te_2Se 44

5.1.2 The LDOS measurement of Bi_2Te_2Se 46

5.2 Imaging qusiparticle interference in Bi_2Te_2Se 47

5.3 Hexagonally warped topological surface state of Bi_2Te_2Se 51

5.4 Ab initio studies on Bi_2Te_2Se 56

5.5 Conclusion 61

6 Conclusion 62

Bibliography 64

List of publications 72

Acknowlegement 73

1 Introduction

Three-dimensional topological insulators (3D TIs) represent a recently discovered state of matter, whose hallmark is the surface state in the absolute bulk energy gap, accompanying a spin non-degenerate Dirac-cone energy dispersion and helical spin texture. The topological surface state (TSS) is protected by time-reversal symmetry and is robust against nonmagnetic perturbations. These unique electronic structure and spin texture of TSS provide a venue not only to explore novel quantum phenomena in fundamental physics but also to show potential applications in spintronics and quantum computing [1–8].

As useful surface-sensitive techniques, angle-resolved photoemission spectroscopy (ARPES) and its spin resolved version (SARPES) are widely used to identify and characterize surface states of the TIs. Some of their peculiar properties have been revealed by one of the most powerful surface probes, scanning tunneling microscopy/spectroscopy (STM/STS) providing direct information on the electronic structure of topological surface states and their scattering properties. Standing waves caused by scattering off from line defects or point like impurities on the surface of 3D TIs is an effective way to present the topological nature of the surface states. The interference between incoming and outgoing waves at a specific momentum leads to an oscillation in the local density of state (LDOS). One can unveil the spin structure of surface states through the presence or absence of standing waves both for occupied and unoccupied states. Meanwhile, the surface energy band structure was determined by employing $k.p$ theory and first principle calculations to explain the experimental data.

Interband optical excitation of topological surface states by pulsed laser light is expected to generate longer lived spin-polarized carriers at the surface [9, 10]. To understand the photo-excited spin and charge dynamics, knowledge of unoccupied topological surface state far above the Dirac point and the unoccupied bulk continuum

is crucial. Note that photoelectron spectroscopy, with which most of the studies on topological insulators have been performed, cannot access unoccupied states or provide direct information on the in-plane electron scattering. Thus, there has been a dearth of measurements on the unoccupied electronic states of 3D TIs, and the present study is motivated by the necessity of getting the information about the unoccupied spectrum.

In this thesis, we focus on the topological nature of surface state and electronic structure of 3D TI Bi_2Te_2Se by using STM/STS and ARPES measurement in a wide energy region combined with theoretical results. The second chapter is devoted to the theoretical background of this thesis. We explain basic principle of STM/STS and ARPES as well as electronic structure calculation. In Chapter 3, we present the history of topological insulator and recent experimental and theoretical progress on two and three-dimensional topological insulators. Chapter 4 provides an introduction to the experimental techniques related to the present work. The main part of this thesis, which named chapter 5, detailed the experimental and theoretical results on the surface of Bi_2Te_2Se are shown. Here, we present the TSS scattering due to strong warping effect in unoccupied state. Chapter 6 gives a brief conclusion of results with a discussion of future directions.

2 Theoretical Backgrounds

2.1 The Scanning Tunneling Microscopy/Spectroscopy (STM/STS)

Nanotechnology is the study of phenomena and fine-tuning of materials at atomic, molecular and macro-molecular scales. It has the potential to meet many of the greatest global challenges in science, medicine, energy and industry. Areas of physics such as nano-electronics, nano-mechanics, nano-photonics and nano-ionics have evolved during the last few decades to provide a basic scientific foundation of nanotechnology. As the practical application of the developments of "Nanotechnology", the invention of the scanning tunneling microscope in 1981 provided unprecedented visualization of individual atoms and bonds by Binnig and Rohrer at the IBM research laboratories in Zürich [11, 12]. The scientific impact of STM was widely recognized, in 1983, Binnig and Rohrer succeeded in producing an atomic resolution image of two unit cells on the 7×7 reconstruction surface of Silicon (111) and captured the attention of the surface science world and resulted in their receiving the Nobel Prize in physics only four years after the invention [13].

2.1.1 Tunneling current

STM in a real space, surface imaging technique based on the quantum mechanical tunneling of electrons between a conducting sharp tip and a metallic or semiconducting surface. Although classically forbidden, tunneling of electrons between tip and sample is allowed in quantum mechanics even before tip and sample come into contact. The wavelike nature of electrons allows for tunneling from one conductor to another through a classical barrier such as vacuum. Instead of solving the Schrödinger equation for a coupled system of tip and sample, Bardeen solved at first

the Schrödinger equation of the subsystems and calculated then using time dependent perturbation theory the transition from one electrode to the other. The tunneling current is given to the first order in Bardeen's [14] formalism by:

$$I = \frac{2\pi e}{\hbar}\sum_{\mu,v}\rho_t(r,E_\mu)\rho_s(r,E_v+eV)f(E_\mu)\,[1-f(E_v+eV)]\left|M_{\mu v}\right|^2\delta(E_\mu-E_v) \tag{2.1}$$

where $f(E)$ is the Fermi function, V is the applied bias voltage and $M_{\mu v}$ is the tunneling matrix element between tip and the sample, which have a local density of states $\rho_t(r,E_\mu)$ and $\rho_s(r,E_v+eV)$, respectively. Since the experiments are performed at room temperature or below and at small voltage, need to consider the limits of small voltage and temperature,

$$I = \frac{2\pi}{\hbar}e^2V\sum_{\mu,v}\rho_t(r,E_\mu)\rho_s(r,E_v+eV)\left|M_{\mu v}\right|^2\delta(E_v-E_F)\delta(E_\mu-E_F), \tag{2.2}$$

If the tip wave functions are randomly localized, then the matrix element is simply proportional to the amplitude of the ψ_v at the position $\vec{r}_0$ of the tip, and (2.2) be reduces to,

$$I \propto \sum_v|\psi_v(\vec{r_0})|^2\,\delta(E_v-E_F), \tag{2.3}$$

The quantity on the right side is simply the surface local density of states (LDOS) at E_F. Thus the tunneling current is proportional to the surface LDOS at the position of the point probe, and the microscope image represents a contour map of constant surface LDOS.

To deal with (2.2) in general, the essential problem is to calculate tunneling matrix element, Bardeen [14] has shown that,

$$M_{\mu v} = \frac{\hbar}{2m}\int d\vec{S}\,.\left(\psi_\mu^*\vec{\nabla}\psi_v - \psi_v\vec{\nabla}\psi_\mu^*\right), \tag{2.4}$$

where the integral is over any surface lying entirely in the vacuum barrier region separating the two sides. To evaluate $M_{\mu v}$, the surface wave function is expended as

$$\psi_v = \Omega_s^{-1/2} \sum_G a_G \exp[\left(k^2 + \left|\vec{k}_G\right|^2\right)^{1/2} z] exp\left(i\vec{k}_G . \vec{X}\right), \tag{2.5}$$

Here Ω_s is sample volume, $k = \hbar^{-1}(2m\phi)^{1/2}$ is the minimum inverse decay length for the wave function in vacuum, ϕ is the work function, and $\vec{k}_G = \vec{k}_{\|} + \vec{G}$, where $\vec{k}_{\|}$ is the surface Bloch wave vector of the state, and $\vec{G}$ is a surface reciprocal-lattice vector. The first few a_G are typically of order unity. For the non-periodic surface the sum over G becomes an integral.

The microscopic structure of the tip is modelized as a locally spherical well where it approaches nearest to the surface, see in Fig. 2.1(a). R is the local radius of curvature about the center located at $\vec{r}_0$, and z is the distance of nearest approach to the surface. The wave functions of the tip are taken to have the asymptotic spherical form,

$$\psi_\mu = \Omega_t^{-1/2} c_t k R e^{kR} (k|\vec{r} - \vec{r}_0|)^{-1} e^{-k|\vec{r}-\vec{r}_0|}, \tag{2.6}$$

where Ω_t is the tip volume and k is defined as above [15]. In practice, the relation for

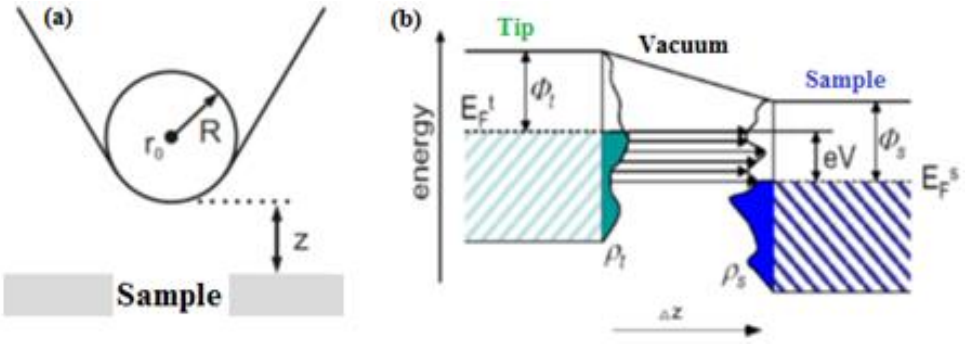

Figure 2.1: (a) Schematic picture of the tunneling junction (Taken from [15]). (b) The energy level diagram for an elastic electron tunneling configuration (Taken from [17]).

one dimensional tunneling is a good approximation to the height dependence of the tunneling current in an actual STM experiment, although for a more exact description refinements should be made to take into account for instance a difference in the work function of the sample and the tip. In order to arrive at an expression for the bias voltage dependence of the tunneling current, in addition to the barrier height dependence described by Equation (2.3), Fermi's golden rule is commonly used to describe electron transitions within perturbation theory [16]. By applying a positive sample bias voltage V, the Fermi energy of the tip is raised with respect to the Fermi energy of the sample by eV, where e is the electron charge, as shown in Fig. 2.1(b). This enables tunnel electrons from occupied states of the tip into unoccupied states of the sample through the tunneling barrier with the width Δz [17]. Electrons from higher energy levels are more likely to tunnel because of the reduced barrier height. However, in tunneling experiments, electrons do not escape into vacuum, but tunnel from one material to another with a vacuum in between. The apparent barrier height will then be equal to the average of the work functions of the two materials [25, 17]:

$$\phi = (\phi_t + \phi_s)/2, \tag{2.7}$$

A work function extracted from the tunneling experiments has been shown to be independent of the tip-to-sample separation as long as this separation is not in the point contact regime [18]. Since the barrier height is a material dependent property, the STM is in principle capable of determining what element resides at the surface of a material. As most materials have a similar work function, and different tips can have different work functions, this is unfortunately rather intricate in practice.

However, the average barrier height from measurements on several samples with several tips can give a good indication of the surface atomic character. Moreover, from the comparison of work functions of different surface structures on the same material measured with the same tip, one can decide if the different surface structures

are due to a different surface atom. In a real life STM experiment, the barrier is not uniform, the shape and orbital character of the tip have to be taken into account to be able to describe the current in detail.

2.1.2 Working principle of STM

The STM structure is an intricate assembly of piezo ceramic motors and other electronics. A signal is applied to the piezo motors providing slip and stick movement in three axis directions, on the angstrom scale. Piezo electric ceramics are attached to the tip. An atomically sharp tip is brought close to the surface of the scanned material by the way of the piezo motors, until a desired tunneling current is established. The

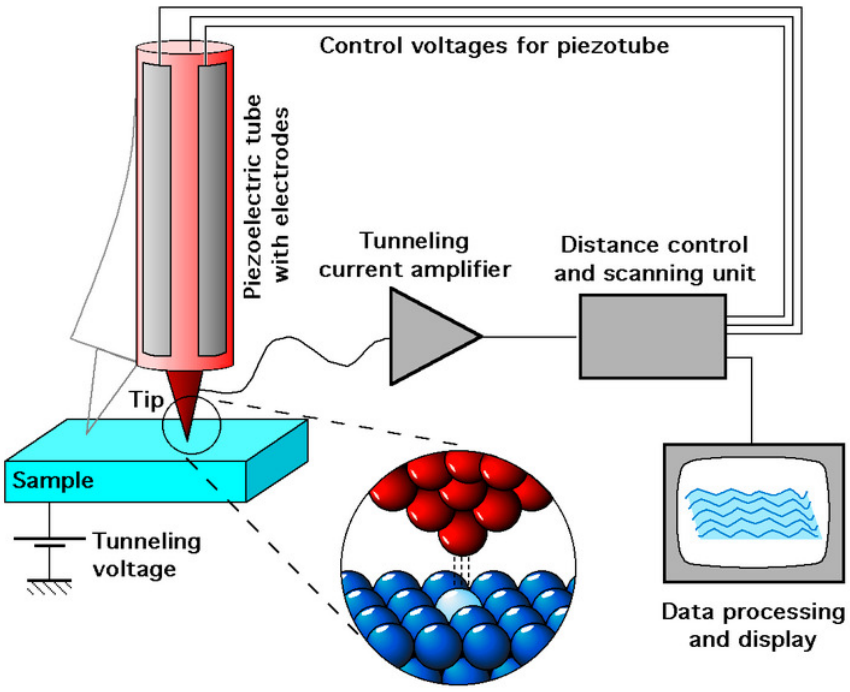

Figure 2.2: Schematic illustration of an experimental STM configuration consisting of the sample of interest, the tunneling tip, the piezoelectric tube that allows the scanning in x-y direction and controls the vertical distance z, and the control unit (Taken from [21]).

electron wave functions in the tip overlap with the electron wave functions in the sample surface. By applying a bias voltage between the tip and the sample, the

"tunneling current" flows in if the tip is contact to the sample (see Fig. 2.2).

When the polarity of sample bias voltage is changed, the tunneling current moves towards to different directions [see Fig. 2.3]. For zero bias voltage applied between tip and sample, the Fermi levels of the tip and sample are aligned at equilibrium, the electrons cannot flow in either direction since the Fermi level (E_F). If the bias voltage $V_{bias} > 0$, the Fermi level of the sample is raised by V_{bias}, the electrons are tunneling from the occupied states of the sample into the empty states of the tip. If $V_{bias} < 0$, the electrons are tunneling from the occupied states of the tip into the empty states of the sample. As the tip scans on the surface of samples, the tunneling current is converted to a voltage by the current amplifier, which is then compared with a reference value. The difference is amplified to drive the *z* piezo. The tip is scanned in the *x*-*y* plane above the sample using the *x* and *y* piezos, while its height is controlled

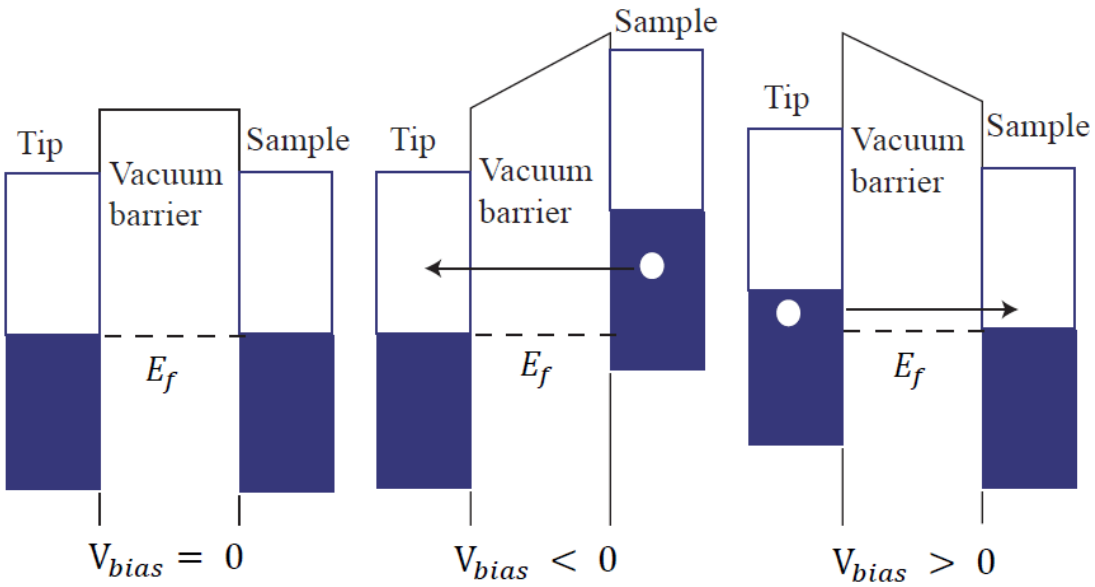

Figure 2.3**:** Schematic relationship of the energy level between tip and sample with different sample bias voltages. The blue and white areas represent occupied and unoccupied states.

using the *z* piezo. Results of a contour plot of the equal tunneling-current surface, is

obtained, displayed, and stored in the computer memory. A scanning tunneling microscope offers a possibility to collect topographic and spectroscopic data on a local scale. In the topographic mode, the surface is mapped via the dependence of the tunneling current through the vacuum barrier that exponentially depends on tip-sample distance z. With the help of the tunneling current the feedback electronic keeps the distance between tip and sample constant. Moving the tip closer or farther to the surface keeps the current constant. This mode is known as the constant current mode [see Fig. 2.4(a)]. The position of the tip is recorded and used to develop the topographic image on the surface. Since the tunneling current integrates over all states above or below E_F, up to energy equal to the tunnel voltage, the current mapping corresponds to a profile of constant integrated electron density of states (DOS). If the LDOS is homogeneous over the mapped area, this profile corresponds to constant tip-to-sample spacing, and recording the height of the tip as a function of position gives a three-dimensional image of the surface $z = z(x, y)$. A second mode is called constant height mode and used less frequently. In constant height mode the tip-sample distance is not adjusted while the tip scans across the surface and the variation of the tunneling current is detected [see Fig. 2.4 (b)]. For the ideal tip and sample, modulations of the

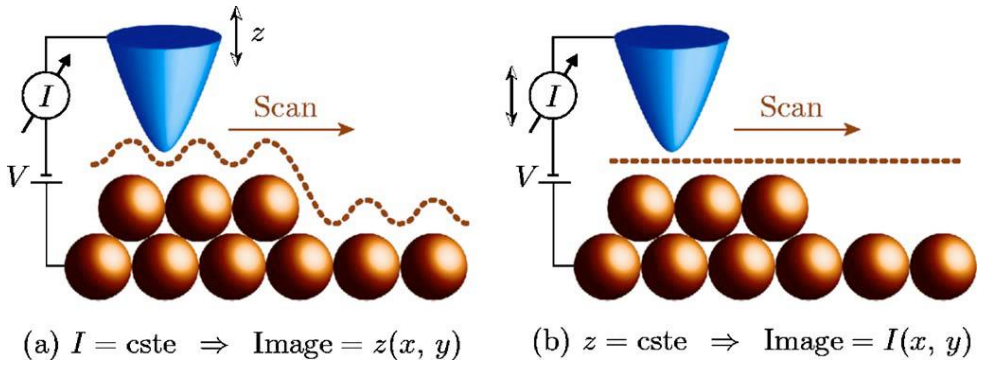

Figure 2.4: Generic STM operating modes: (a) constant-current and (b) constant-height imaging (Taken from [22]).

tunneling current $I(x, y)$ are due only to variations in the tip-to-sample spacing, and

recording the current as a function of position will reflect the surface topography. This mode allows fast scanning, but is restricted to surface areas where corrugations do not exceed a few angstroms, to avoid tip collisions with large surface protrusions. So, the constant height mode can only be applied on flat surfaces with low corrugation and well leveled tip surface geometries, otherwise the tip crashes, destroying both the tip and the sample surface.

2.1.3 Scanning tunneling spectroscopy (STS)

In addition to imaging the surface topography with atomic-scale resolution, scanning tunneling microscope also allows one to probe the local electron density of states (LDOS) with exceptional spatial resolution and well-controlled tunneling barriers. Scanning tunneling spectroscopy (STS) experiments are usually performed to get more information out of the measurement than just a topographic image. The advantage of STS is the high lateral resolution. The differential conductance (dI/dV) is proportional to the LDOS of the sample when the tip-sample distance is constant, and the LDOS is energetically resolved. In spectroscopy, the LDOS of the material is extracted through measurements of the tunneling conductance, the tip is positioned at an interesting spot on the surface after the feedback loop is opened, the bias voltage is swept over the energy range of interest and the current is recorded.

Considering a free-electron metallic tip, the DOS of the tip can be proximately regarded as constant in the energy region of interest. Thus the tunneling current is proportional to the integrated DOS of the sample only:

$$I \propto \int_0^{eV} \rho_s(E_F + eV)\, d\varepsilon, \tag{2.8}$$

The first derivative of the I(V) curve gives information about the charge density distribution of a sample surface. The first derivative of equation (2.8) is:

$$\frac{dI}{dV}(V) \propto \rho_s(x, y, E_{F,t} + eV), \tag{2.9}$$

There are several ways to obtain the dI/dV spectroscopy data such as numerical differentiation of I(V) curves or a lock-in amplifier technique. For a lock-in technique, the dI/dV image is measured simultaneously with the topography image using a lock-in amplifier. A modulation signal with a small amplitude and a high frequency is added to the bias voltage, and its response to the tunneling current is measured. The lock-in amplifier combines these two signals, and the output corresponds to the derivative dI/dV. In this way the LDOS at position (x, y) on the surface can be measured. Therefore, a measurement of dI/dV as a function of sample bias V allows in principle to measure the sample LDOS in a given energy range close to the Fermi energy. The situation is however complicated by the fact that the tunneling transmission probability is bias dependent. This non-constant contribution of the tunneling transmission probability to a dI/dV spectrum can be corrected to some extend by an appropriate normalization procedure. However, for the numerical method, typically measure an I(V) curve at every pixel on a two-dimensional grid is performed. The I(V) curves are numerically differentiated after the actual measurement and in this way, the three-dimensional data set: dI/dV (x, y, V) can be obtained.

2.2 Angle-resolved photoemission spectroscopy (ARPES)

The macroscopic properties of solids are governed by their microscopic electronic structures, therefore is important to study its electronic structure in order to understand, control or make use of the novel physics in various advanced materials. For some decades now, photoelectron emission spectroscopy (PES) and angle-resolved photoemission spectroscopy (ARPES) have been used to study the electronic structure of strongly correlated electron materials in condensed matter [23-29]. But

PES is not-able for its surface sensitivity. It allows to probe surface-related electronic states, but it also restricts the method to detecting only the surface part of a general bulk contribution. ARPES can directly detect the band structures of materials. This unique advantage, together with its broad applicability to various material systems, has made ARPES a technique to play an important role in the study of novel materials.

2.2.1 Photoelectron emission spectroscopy (PES)

Photoelectron Emission Spectroscopy (PES) has been established as one of the most important methods to study the electronic structure of molecules, solids and surfaces [23, 24]. Historically the first experiment that revealed the interaction of light

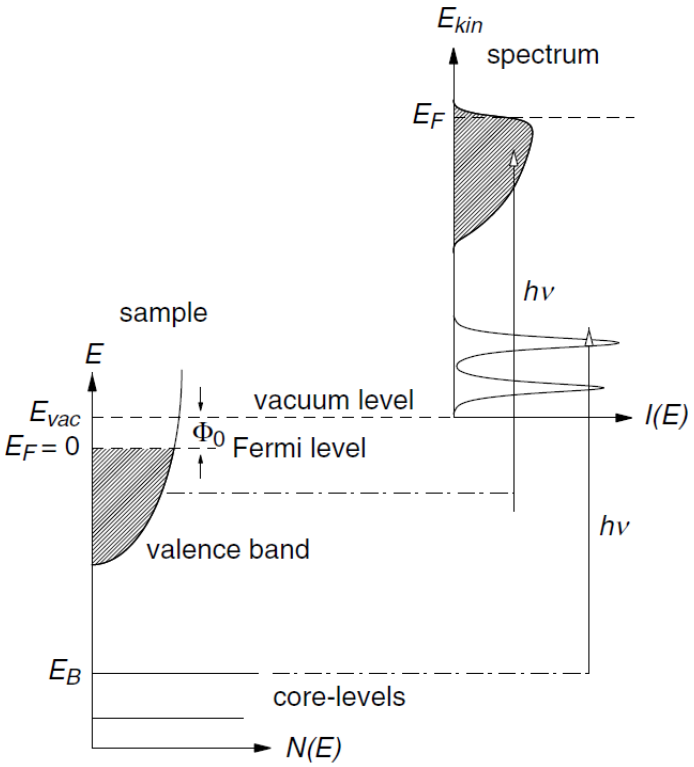

Figure 2.5: Schematic view of the photoemission process in the single-particle picture. Electrons with binding energy E_B can be excited above the vacuum level E_{vac} by photons with energy $h\nu$ (Taken from [28]).

with solids, which is known today as the photoelectric effect, were performed by H. Hertz and W. Hallwachs in 1887 [25, 26] and later explained as a manifestation of the quantum nature of light by Albert Einstein in 1905 [27]. The basic principle of PES consists of irradiating the sample with ideally monochromatic photons and measuring the kinetic energy spectrum of the emitted electrons.

When an electron in solid is ejected by light which has larger energy than the work function ϕ, the electron escapes from the surface of the solid, knowing its kinetic energy E_{kin}^{V}, and applying the energy conservation law, one can determine how strong the electron is bound to the material:

$$E_{kin}^{V} = hv - E_B - \phi, \tag{2.10}$$

where hv is the energy of the incident photon and E_B is the binding energy of the electron relative to the Fermi level E_F. In practical PES experiments, since both a sample and an electron energy analyzer are grounded, the kinetic energy of the photoelectrons E_{kin} is referred to E_F. Thus, we obtain,

$$E_{kin} = hv - E_B, \tag{2.11}$$

the energy $-E_B$ is regarded as the energy of the electron inside the sample material before the emission. Therefore, the energy distribution of the electron inside the material can be directly mapped out as the distribution of the kinetic energies of the photoelectrons. If we fix the energy of the incident photon and record the count of photoelectrons as a function of kinetic energy, we obtain a photoemission spectrum.

Fig. 2.5 schematically illustrates how the electronic density of states is mapped out as energy distribution curve (EDC) that is called the photoemission spectrum. A detailed analysis of the PES data allows the determination of the elemental composition of the surface and of the atom coordination in terms of geometrical structure and chemical bonding. Furthermore, PES has widespread practical

implications in various fields like surface chemistry or material science, and has significantly contributed to the understanding of fundamental principles in solid state physics.

2.1.2 Angle-resolved photoemission spectroscopy

Angle-resolved photoemission spectroscopy (ARPES) has proven to be one of the most powerful experimental techniques for measuring the distribution of photo-ejected electrons with respect to kinetic energy and small acceptance angle about the sample surface normal. Being the same as PES, ARPES removes electrons via the photoelectric effect. Photoelectrons are stimulated by incident photons and escape outside of material into the vacuum, and they are counted by an angle resolved electron energy analyzer [29]. As long as the electron is able to leave the material without colliding with any other electrons, its momentum is preserved. The energy and momentum of the ejected electrons are measured with a hemispherical electron spectrometer. The momentum of photoelectrons could be calculated by

$$P = \sqrt{2mE_{kin}}, \tag{2.12}$$

in which m is the mass of electron. In an ARPES experiment what is measured is not only the intensity as a function of kinetic energy, but also as a function of the photoemission angle. The momentum components of parallel and perpendicular to sample surface are determined by the polar angle θ and azimuthal angle φ of the sample. For the light source used in ARPES experiments, the momentum of the photon is negligible compared to that of electron, so the energy and momentum of photoelectrons, binding energy and crystal momentum in solids could be related by

$$P_{\parallel} = \hbar k_{\parallel} = Psin\theta = \sqrt{2mE_{kin}}sin\theta, \tag{2.13}$$

where the $\hbar k_{\parallel}$ is the component of electronic crystal momentum parallel to surface in the extended Brillouin zone.

The momentum and energy relation for the individual components, according to their emission angles in spherical coordinates are as follows:

$$k_x = \sqrt{2mE_{kin}/\hbar^2}\, sin\theta cos\varphi, \tag{2.14}$$

$$k_y = \sqrt{2mE_{kin}/\hbar^2}\, sin\theta sin\varphi \tag{2.15}$$

$$k_z = \sqrt{2mE_{kin}/\hbar^2}\, cos\theta \tag{2.16}$$

In the process of photoemission, total energy and momentum parallel to the surface are conserved, but the momentum perpendicular to the sample surface is not conserved because of the broken of translational symmetry along this direction. A plot of photocurrent as a function of energy for a fixed (k_x, k_y) is called the energy distribution curve (EDC), while the momentum distribution curve (MDC) refers to the photocurrent as a function of $k_{\parallel}$ at a fixed energy E_B.

Performed with high energy and angular resolutions, ARPES is able to measure details of the electronic structure such as the Fermi surface and energy-band dispersion. ARPES is thus unique in its ability to probe the valence electrons and their energy and momentum dependent band structure whereas the correlated behaviors. In this way, ARPES has played a fundamental role in critical avenues of progress in condensed matter physics. However this technique can only measure occupied single electron states. To measure the unoccupied states, or excitations, there is inverse photo-emission spectroscopy (IPES) as well as tunneling experiments [30].

2.1.3 Synchrotron radiation

Due to the production of high flux and continuum energy in photon beams, the first

studies on the electronic structure of a solid using ARPES were not performed until the mid 1970's [28]. Synchrotron radiation facilities have overcome this problem supplying bright photon beams with continuum energy from the infrared to the x-ray regime, and have been used as the photon source in spectroscopic experiments.

Synchrotron radiation facility consists of a linear accelerator for the initial acceleration, an injection ring used to accelerate electrons near the speed of light, a storage ring typically on several hundred meters in diameter, bending magnets to focusing electron beam. The acceleration of the electrons in the bending magnets produces a tangential photon beam. The emitted light from these devices is later monochromatized and directed to the experimental chamber by means of gratings and mirrors [31, 32]. The whole system is kept in an ultra-high vacuum.

Thus the synchrotron radiation serves as an ideal light source for the ARPES experiment, which enables the experimental measurement in the three dimensional *k*-space. Moreover by changing the photon energy, the kinetic energy of the photoelectrons is also varied, which can be utilized to selectivity change the surface or bulk sensitivity of ARPES experiment.

2.3 Electronic structure calculations

Nowadays, density functional theory (DFT) is by far the most widely used approach for electronic structure calculations. It is usually called first principle calculation or ab initio (slab) calculation, because it allows one to determine many properties of condensed matter systems by just giving some basic structural information without any adjustable parameters. It provides an alternative way to investigate condensed matter systems, other than the traditional experimental method and pure theoretical method based on quantum (field) theory. The main idea of DFT is to describe a many-body interacting system via its particle density and not via its many-body wave function. Its basis is the well-known Hohenberg-Kohn (HK) theorem [33], which

claims that all properties of a system can be considered to be unique functional of its ground state density.

By construction DFT is a method to obtain the electron density and the total energy of a many-body system in its ground state. In order to study surface properties, one usually works with the slab geometry. For slab calculations, the convergence of surface properties with respect to the number of bulk layers and the vacuum thickness must further be verified. The number of layers must be chosen sufficiently large to avoid that opposite surfaces interact. The number of vacuum layers is chosen such as to minimize the overlap of evanescent waves from surfaces of neighboring slabs. Within density functional theory, this leads inevitably to a higher number of bands and back folding of bands. However, in real experiments, it is only the surface periodicity which gets larger, whereas the bulk periodicity remains unchanged. Thus the bulk bands are not expected to back fold. Within a given symmetry some structural degrees of freedom may be available during relaxation, however alternative or lower symmetries must be considered. Even the number of surface atoms may differ between physically plausible structures. It is therefore imperative that as many structures as practicable are compared to as many experimental results as possible, before a particular model may be accepted. It is becoming a useful tool used by both experimentalists and theorists to understand characteristic properties of materials and to make specific predictions of experimentally observable phenomena for real materials and to design new materials.

Despite the improvements in DFT, there are still difficulties in using DFT to properly describe intermolecular interactions, charge transfer excitations, transition states, global potential energy surfaces and some other strongly correlated systems, and in calculations of the band gap of some semiconductors. A common problem is that theoretical band gaps often come out much smaller than in experiment. This works usually quite well for occupied states, but is generally less reliable for empty states.

3 Topological insulators

Topological insulator (TI) is an unusual class of quantum state and has attracted great deal of attention in condensed-matter physics due to its fascinating physical properties and potential technological applications in spintronics and quantum computing [1-5]. Like ordinary insulators, topological insulators possess a bulk energy gap separating the filled valence bands and the empty conduction bands, but have protected conducting states on their edge [two dimensional (2D) TI] or surface [three dimensional (3D) TI].

The history of TIs started from the discovery of quantum Hall effect (QHE) [34] in the 80s, known as topological phases determined by the topology in their ground state, in the sense that certain quantities are invariant under small perturbations and cannot change without closing the energy gap of excitations in the bulk of the material.

As a new family of topological phases, the TIs in 2D and 3D were proposed theoretically [35-38] then followed by experimental realization [39-43]. The TIs generated by a spin-orbit coupling (SOC) are invariant under time-reversal (TR) symmetry. The Z_2 invariants of a crystal determine the transitions between ordinary and topological insulators as its bands are occupied by electrons. In two dimensions, the quantum spin Hall phase is distinguished from a band insulator by a single Z_2 invariant [36] whereas four Z_2 invariants are used in three dimensions [3, 44]. These topological effects have been found to exist in common compounds such as Bi-based chalcogenides, formerly known for infrared detection or thermoelectric applications, without any requirements of extreme conditions such as high magnetic fields or low temperatures.

3.1 Topological phase of quantum matter

A topological phase is defined as a quantum-mechanical phase of matter where the ground state shows a gap. The topological band theory can be applied not only to insulators but also to superconductors [1, 4]. Topological phase of quantum matter now offers a new platform to test some of the exotic ideas in mathematics and physics. Recently two topological phases of quantum matter have been experimentally discovered—the quantum Hall and the quantum spin Hall states—one may naturally wonder about how they would fit into a bigger unifying picture [34, 39].

3.1.1 Quantum Hall effect (QHE)

One of the greatest achievements of modern physics is the discovery of the integer quantum Hall effect in 2D electron gases by von Klitzing in 1980 [34]. The QH effect was the first phase that no spontaneously broken symmetry existed. In the integer quantum Hall effect [34, 44-46], an energy gap results from the quantization of the closed circular electron orbits under a magnetic field. An insulator is described by a gapped band Hamiltonian with a non-zero energy gap separating the occupied and unoccupied conducted bands [see Figs. 3.1(a) and (c)]. While the kinematics of quasi-particles, such as the effective mass tensor, is described by the dispersion of the band spectrum, the topology of an insulator is encoded in its Bloch functions [1]. It reflects certain robust properties of the material that cannot be changed without going through a metallic transition that closes the energy gap.

The quantum Hall effect requires inherently a quantum mechanical description of the electrons in two dimensions. The inside of a quantum Hall system is thus inert like an insulator. However at the boundary of the material a different type of motion occurs, which allows electron to flow in one-dimensional edge states. The QH state features gapless chiral edge states, either spin up or down, depending on the direction of the

magnetic field only. If we were to switch off the magnetic field, the material would go into an ordinary (trivial) metallic state [see Figs. 3.1(b) and 3.1(d)].

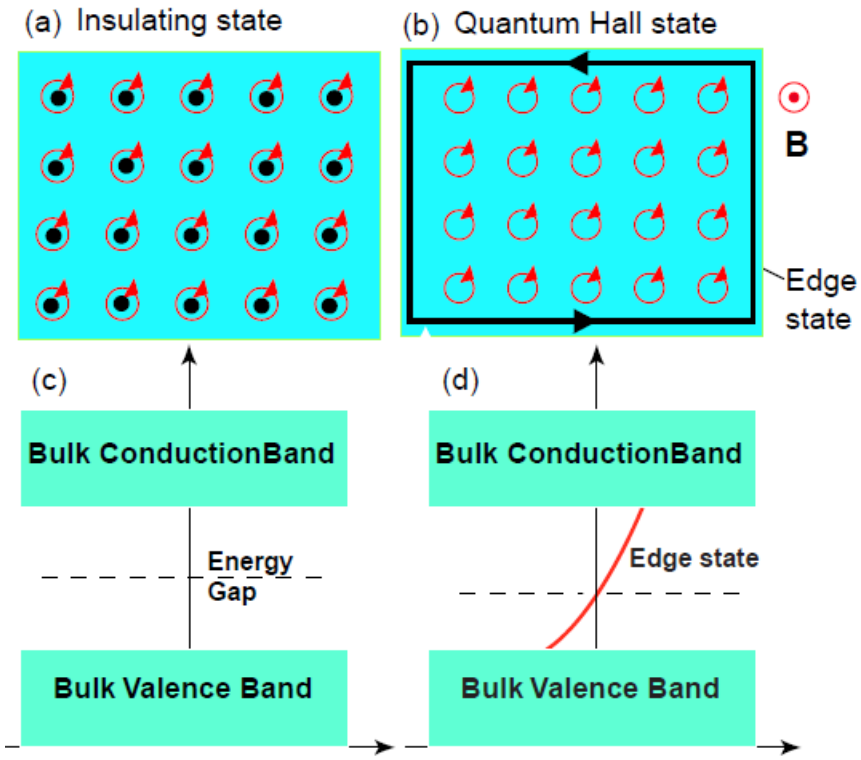

Figure 3.1: (a) An atomic insulator and its insulating band structure (c). (b) The two-dimensional quantum Hall state in a strong magnetic field and its band structure which has a bulk energy gap like an insulator but permits electrical conduction in one-dimensional "one way" edge states along the sample boundary (d).

The conductivity of QH states can be expressed using the Kubo formula of linear response theory as an integral involving valence band states. This state is created by confining electrons into two dimensions and subjecting them to a strong perpendicular magnetic field arising Landau levels splitting and an in-plane electric field. Unlike an insulator, though, an electric field causes the cyclotron orbits to drift, leading to a Hall current characterized by the quantized Hall conductivity,

$$\sigma_{xy} = Ne^2/h, \tag{3.1}$$

where N is an integer which is known as the TKKN invariant, e is the electron charge and h is Planck's constant. The topology of occupied bands is determined by the TKNN integer N, also called as the first Chern number. This integral invariant carries only information about the occupied states, therefore is insensitive to perturbations that alter the energy spectrum of the system. The Chern invariant is the total Berry flux in the Brillouin zone,

$$n_m = {}^{1}/_{2\pi} \int d^2\vec{k}\, \mathcal{F}_m, \tag{3.2}$$

n_m is integer quantized for reasons analogous to the quantization of the Dirac monopole and $\mathcal{F}_m = \nabla \times \mathcal{A}_m$ is so-called the Berry curvature while $\mathcal{A}_m$ is the well-known Berry connection. The total Chern number, summed over all occupied bands, $n = \sum_{m=1}^{N} n_m$ is invariant even if there are degeneracies between occupied bands, provided the gap separating occupied and empty bands remains finite and helps to explain the robust quantization of σ_{xy} [1, 4].

Graphene is a single layer of graphite, which is known as a simple example of the QHE in a band theory provided in a periodic magnetic field [47]. The conduction band and valence band touch each other at two specific points in the Brillouin zone. The simplest description of graphene with Bloch Hamiltonian is:

$$H(k) = h(k) \cdot \sigma, \tag{3.3}$$

where $\vec{\sigma} = (\sigma_x, \sigma_y, \sigma_z)$ are Pauli matrices and $h(k) = (h_x(k),\ h_y(k), 0)$. The Dirac points emerge because the two components $h(k)$ can have point zero in two dimensions and the degeneracy at the Dirac point is protected by $\mathcal{P}$ and $\mathcal{T}$ symmetries. By breaking these symmetries the degeneracy can be lifted. For instance, $\mathcal{P}$ symmetry is violated if the two atoms in the unit cell are inequivalent. This allows $h_z(k)$ to be

nonzero. If $h_z(k)$ is small, then form (3.3) becomes a massive Dirac Hamiltonian near K,

$$H(q) = \hbar v_F q \cdot \vec{\sigma} + m\sigma_z, \tag{3.4}$$

where $m = h_z(K)$. The dispersion

$$E(q) = \pm\sqrt{|\hbar v_F q|^2 + m^2}, \tag{3.5}$$

has an energy gap $2|m|$. Note that $\mathcal{T}$ symmetry requires the Dirac point at K' to have a mass $m' = h_z(K')$ with the same magnitude and sign, $m' = m$. This state describes an ordinary insulator.

The electron transport properties at the surface of a material exhibiting the QHE are independent of scattering rates associated. This is why the surface states that characterize the QHE are extremely robust to scattering impurities in the sample. But, there is experimental requirements, such as strong magnetic fields, very low temperatures as well as crystal purity. The quest for finding a new material system which exhibits the desired robust edge states, without any need for magnetic fields and with the promise of functioning up to room temperature has yielded results in the past few years.

3.1.2 Quantum spin Hall effect (QSHE)

The QH state provided the first example of a quantum state shows an intrinsic topological order which is stable even without any symmetry. Recently, a new class of topological phases has emerged so called quantum spin Hall (QSH) insulators [35]. The QSH insulator is constructed by taking two copies of quantum Hall systems with opposite Chern number and spin, has motivated the study of the symmetry-protected topological order. The QSH phase is a time reversal invariant electronic state with a

bulk electronic band gap that supports the transport of charge and spin in gapless edge states.

In contrast to QH state, the spin-orbit coupling plays an analogous role to the external magnetic field in the quantum spin Hall systems. Time-reversal flips both the spin-up and spin-down electrons as well as the sign of σ_{xy}. As a result, in an applied electric field, the spin-up and spin-down electrons give rise to spin-polarized Hall currents flowing in opposite directions which are referred to as helical edge states, in analogy to the relation between the spin and the momentum of a particle known as helicity from relativistic quantum mechanics (Fig. 3.2).

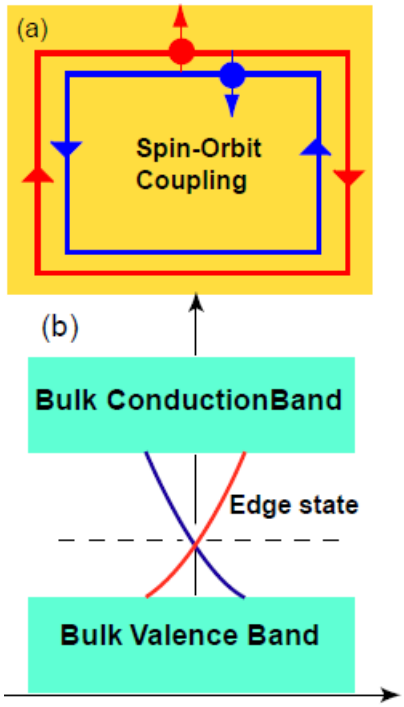

Figure 3.2: (a) Quantum Hall spin state and its band structure (b).

The QSH phase has been first predicted for graphene due to its tiny energy gap, however, its realization in experiment seems to be quite difficult. It would also be of interest to find other materials with stronger SOC which exhibit this effect [35].

3.2 Topological insulators in 2D

HgTe/CdTe quantum wells have been calculated as a first 2D topological insulator and experimentally realized immediately after the prediction [39]. $Hg_{1-x}Cd_xTe$ is a family of semiconductors with strong spin-orbit coupling and has demonstrated

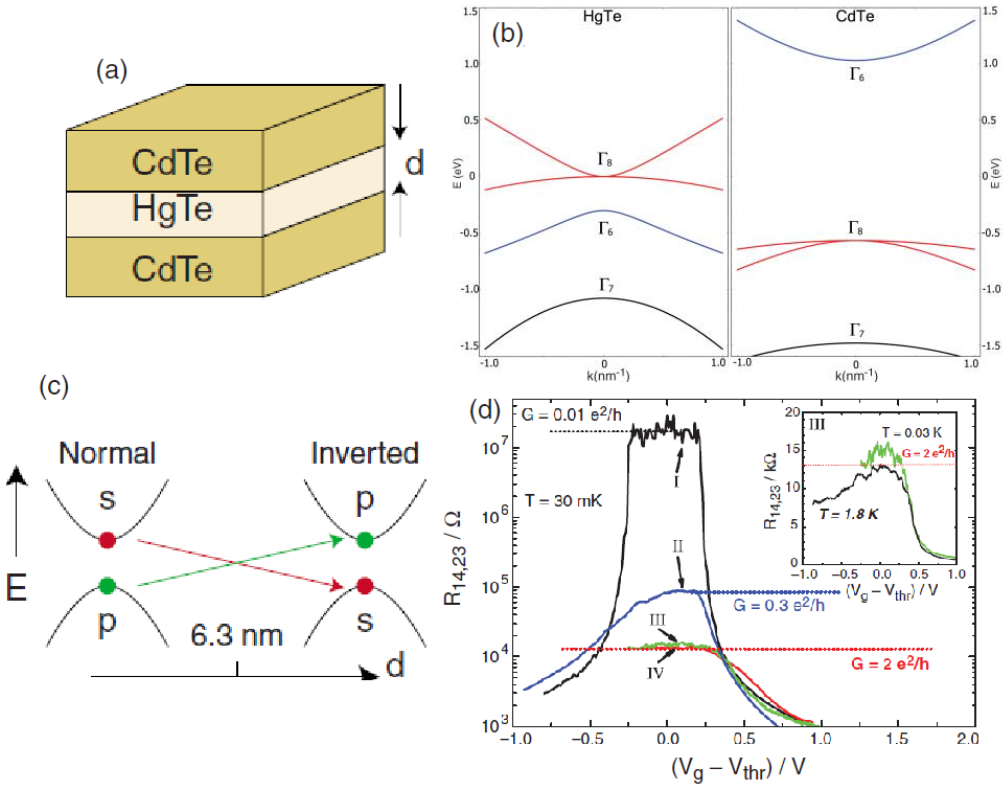

Figure 3.3: (a) Quantum well structure. (b) Bulk band structure of HgTe and CdTe. (c) As a function of layer thickness d the 2D quantum well states cross at a band inversion transition. (d) Experimental visualization of two terminal conductance as a function of a gate voltage that tunes E_F through the bulk gap (Taken from [1, 39]).

quantum phase transition as a function of thickness d_{QW} of the quantum well. CdTe behaves as conventional semiconductors, but their theoretical analysis shows that in an appropriate range of layer thickness this two-dimensional structure should exhibit a robust QSH effect. For both HgTe and CdTe, the important bands near the Fermi level are close tothe Γ point in the Brillouin zone [Fig. 3.3(b)]. They are s-type band (Γ_6), and a p-type band split by SOC into a $J = 3/2$ band (Γ_8) and a $J = 1/2$ band (Γ_7).

Because of the large SOC in the Mercury atom, the usual band ordering is inverted: The negative energy gap indicates that the Γ_8 band, which usually contributed to the valence band, is moved above the Γ_6 band. The light-hole Γ_8 band becomes the conduction band, the heavy-hole band becomes the first valence band, and the s-type band (Γ_6) is shifted below the Fermi level to lie between the heavy-hole band and the spin-orbit split off band (Γ_7). A topological phase transition occurs due to the band inversion at the Γ point driven by the SOC [Fig. 3.3(c)]. Figure 3.3(d) shows the resistivity measurements for a series of samples as a function of a gate voltage which tunes the Fermi energy through the bulk energy gap. In strip geometry with two edges, each edge supports one propagating mode of a given chirality with a conductance e^2/h, hence the predicted longitudinal conductance in such a geometry is $2e^2/h$ [39]. These experiments confirm the existence of the edge states of the quantum spin Hall insulator. Subsequent experiments have established the inherently nonlocal electronic transport in the edge states.

The HgTe/CdTe quantum well is characterized by an insulating gap in the bulk and a single pair of helical edge states at each edge. The helical edge state forms a single 1D massless Dirac fermion with counter-propagating states under TR symmetry.

This leads to searching for new TI materials. Recently, Murakami et al., have theoretically predicted that 2D bismuth shows the QSH effect, because the number of pairs of helical edge states is odd and the Z_2 topological number is nontrivial [48] and Zheng liu et al., demonstrated Bi (111) ultrathin films are characterized by a nontrivial Z_2 number independent of the film thickness [49].

3.3 Topological surface state of 3D topological insulator

Inspired by the discovery of 2D topological insulators, the classification of band structures has been extended to other class of materials in 3D. The existence of 3D topological insulators was predicted by deriving topological invariants for a general

time-reversal-invariant band insulator that displays the band inversion transition. Similar to their 2D counterpart, the bulk states are fully gapped, but there is a topologically protected surface state consisting of an odd numbers of massless Dirac fermions. This phase was predicted in several real materials and the first 3D topological insulator to be experimentally discovered was the semiconducting alloy $Bi_{1-x}Sb_x$, whose unusual surface bands were mapped in an ARPES experiment [41]. On the other hand, this alloy has odd number of surface states whose spin-texture supports a non-trivial Berry's phase providing protection against non-magnetic disorder. While the surface structure of $Bi_{1-x}Sb_x$ alloy material was found to be rather complicated and band gap to be rather small, this work motivated a search for topological insulators with larger band gap and simpler surface spectrum for observing topological phenomena at high temperatures. In 2009 second-generation topological insulators, including Bi_2Se_3, Bi_2Te_3 and Sb_2Te_3 which have numerous desirable properties, were identified experimentally and offer the potential for protected surface states and other topological behavior at room temperature [42-43, 50]. Unlike the multiple branches of surface states observed for $Bi_{1-x}Sb_x$, these experiments report a remarkably simple surface-state spectrum with a single Dirac cone located at the Γ point and a large bulk band gap, in accordance with the theoretical predictions.

Topological surface state (TSS) with a single Dirac-cone energy dispersion and helical spin texture is the manifestation of 3D TIs. TSSs are protected by time reversal symmetry which implies that the surface state Dirac node would be robust in the presence of non-magnetic disorder but open a gap in a broken time-reversal symmetry perturbation of the system such as the effect of magnetic impurities and the associated disorder. Of all the 3D TIs, the most extensively studied is Bi_2Se_3 owing to its large energy gap and the single TSS [42, 51]. However, in spite of significant efforts to realize the surface isolated transport in Bi_2Se_3, the progress has been

hampered by a too small surface contribution to the total conductance compared to the uncontrolled bulk contribution from the carrier doping due to the Se vacancies [52, 53].

In Bi_2Te_3, an unconventional hexagonal warping effect for energies well above the Dirac point appears due to the threefold symmetric crystal potential, under which the constant energy contour (CEC) of surface band evolves from a convex circle to a concave hexagon. Oscillations of LDOS near a step are analyzed. Within the main part of the surface band oscillations are strongly damped, supporting the hypothesis of topological protection. At higher energies, as the surface band becomes concave, oscillations appear, dispersing with a wave vector that may result from a hexagonal

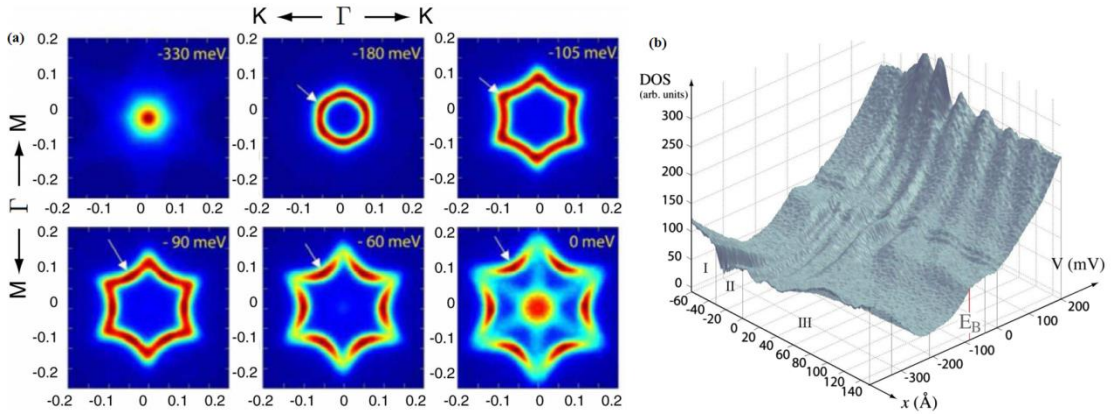

Figure 3.4: (a) Hexagonal warping of surface states in Bi_2Te_3. (b) Averaged spectroscopy as a function of distance from the step (Taken from [54]).

warping term as shown in Fig. 3.4 [54]. Speaking of applications within this class of materials, Bi_2Te_3 is already well known to materials scientists working on thermo-electricity. It is a commonly used thermoelectric material in the crucial engineering regime near room temperature.

The 3D TIs, has generated widespread research activity in condensed matter and material physics communities, there has also been intense efforts to extend the search for topological insulators from the binary Bi-based series to the ternary compounds.

In this thesis we focus on Bi_2Te_2Se, which has been theoretically predicted to be a 3D TI [55] and confirmed by ARPES [56–58]. Figure 3.5(a) shows the single Dirac cone with linear dispersion at the $\bar{\Gamma}$ point within the band gap. A highly spin polarized TSS in Bi_2Te_2Se has been observed in recent spin-resolved ARPES (SARPES) measurements [59]. The results clearly show the magnitude of in-plane spin polarization for the surface state reaches 77 %. [see Fig. 3.5(b)].

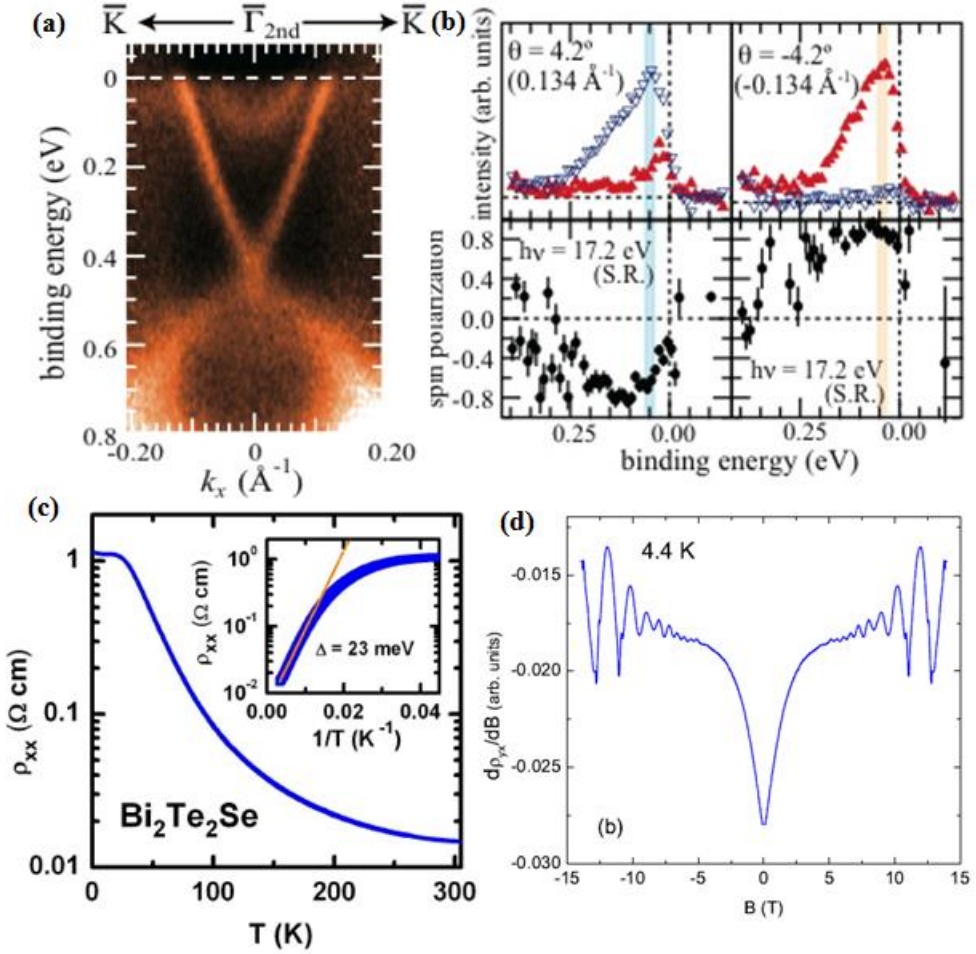

Figure 3.5: (a) ARPES energy dispersion curves of Bi_2Te_2Se along $\bar{\Gamma}_{2nd} - \bar{\Gamma}\bar{K}$. (b) SARPES for Bi_2Te_2Se near E_F (1st BZ) (c) Plot of the resistivity as a function of temperature, inset shows the Arrhenius plot. (d) Displays the prominent SdH oscillations observed in the derivative $d\rho_{xy}/dB$ with magnetic field at 4.4 K (Taken from [59-61]).

Indeed, this compound has been found bulk insulating, and surface-derived quantum oscillations have been observed in a magneto-transport experiment [60, 61]. Carefully

prepared BTS crystals not only present very low bulk conduction, but also show clear Shubnikov-de Haas (SdH) oscillations that reflect a high mobility of surface Dirac electrons as shown in Fig. 3.5(c) and Fig. 3.5(d). The electronic structure of Bi_2Te_2Se closely resembles that of Bi_2Te_3. This makes Bi_2Te_2Se very promising for spintronic applications.

3.4 Backscattering in 3D topological insulators

While the 3D TIs have single Dirac cone surface states with helical spin texture, time reversal symmetry plays an important role. Time-reversal symmetry implies that every spin-half eigenstate is degenerate in energy with, and distinct from, its time-reversal conjugate. The spin direction therefore processes as the electron momentum moves around the Fermi surface. This is often referred to as spin momentum locking. The odd number of crossings protects the surface states from being gapped regardless of the position of the chemical potential or the influence of non-magnetic perturbations. Furthermore, spin-sensitive experiments have established that these surface states have a chiral spin structure and an associated Berry's phase, which makes them distinct from ordinary surface states with strong SOC [4].The robustness of Kramers pairs necessitates that any time-reversal invariant perturbation, such as potential scattering, has a zero matrix element between the two states of a pair, as otherwise it would split the pair.

All these characteristics suggest that backscattering between states of equal and opposite momentum, which results in Anderson localization in typical low-dimensional systems, will not occur for these 2D carriers [see Figure 3.6]. Scattering at any angle other than 180 degrees is allowed.

At low temperatures, the resistivity of a metal is dominated by the scattering of electrons of impurities and imperfections in the metal's crystal lattice. A key predicted

feature for the metallic surface states of topological insulators is their insensitivity to consequently localization. When there are impurities on the surface of a topological

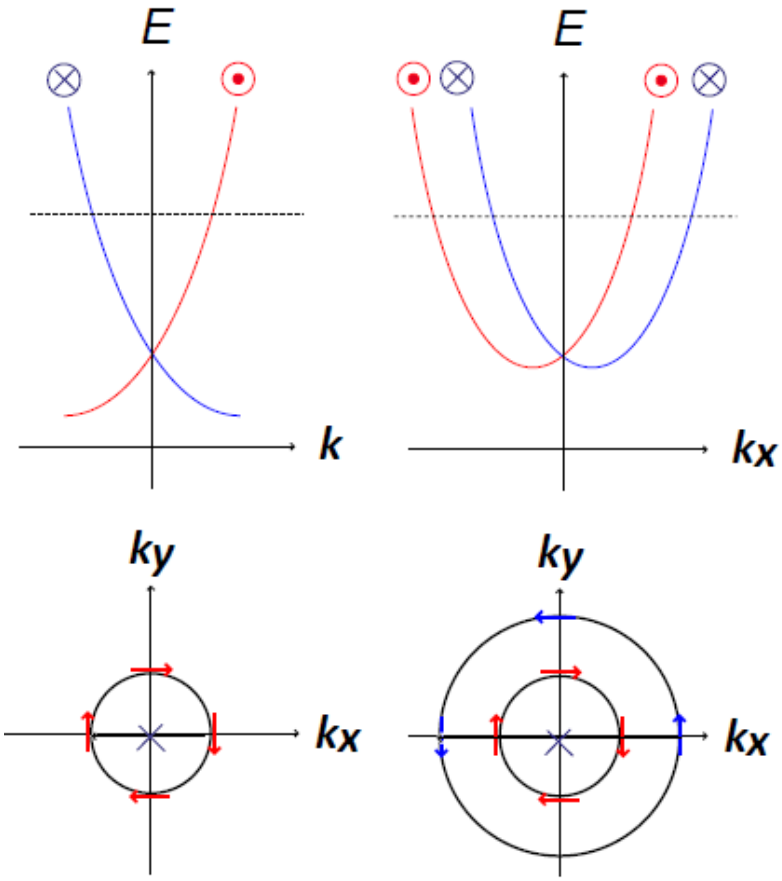

Figure 3.6: Comparison between the Dirac dispersion (left top and bottom) and the dispersion of a 2DEG with Rashba spinorbit coupling (right top and bottom).

spin-independent scattering, which is thought to protect them from backscattering and insulator, the surface states will be scattered and form an interference pattern around the impurities. These properties are reflected on scattering surface state electrons around point defects or impurities through the created standing waves. Fourier transformation of the interference pattern into momentum space, one can quantitatively extract the scattering intensity. Within a simple model of QPI, the interference wave vectors connect regions of high density of states on constant energy

contours. With such information one can determine what types of scattering events are suppressed.

Based on the effective model Hamiltonian, the topological nature of TSS in 3D TI was further performed. For the surface state electrons, the joint density of states (JDOS) as well as the spin dependent scattering probability (SSP), that should QPI patterns without and with spin consideration can be independently determined from ARPES measurements. Remarkably, all the features of the complex QPI patterns and their energy dependence can be understood in detail by the allowed scattering wave vectors based on the band structure of the topological surface states and the spin scattering rule. This agreement provides a precise demonstration that scattering of electrons obeys the spin scattering rules and associated suppression of backscattering.

The electron scattering of point-like impurities and line defects on 3DTI surfaces, make highly relevant for future attempts to design electronic devices.

4 Experimental techniques

The experiments presented in this thesis are performed using a scanning tunneling microscope/spectroscopy (STM/STS) and angle-resolved photoemission spectroscopy (ARPES) in Hiroshima Synchrotron Radiation Center (Hisor). Samples were cleaved at ultra-high vacuum (UHV) *in situ* at room temperature for the STM and at 10-20 K for ARPES measurement.

4.1 Description of the STM system

Our experiments were performed using an LT-STM (Omicron Nanotechnology GmbH) [62]. The base pressure in the STM chamber is better than $1 \times 10^{-9}\ Pa$. Our STM is designed to perform measurements at room temperature (300 K), liquid nitrogen (77 K) and liquid helium (4.5 K). A counter-heating facility (Lakeshore 331) allows accessing a wide range of temperatures. The STM system is combined with

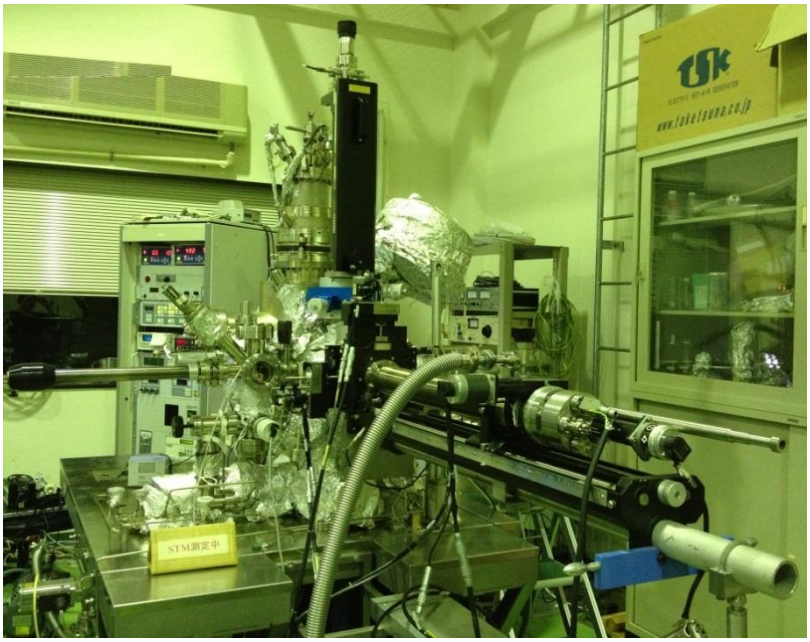

Figure 4.1: The Low-temperature scanning tunneling microscope in Hiroshima synchrotron radiation center.

electron analyzer (SES100) of GAMMADATA-SCIENTA that allows us to do STM and PES measurement with the same sample (see Fig. 4.1). The in-situ low energy electron diffraction (LEED) has been performed to determine the crystallographic orientation of each individual sample that is measured in the STM.

4.1.1 UHV system

Since the STM/STS is one of the most surface sensitive techniques, the measurements have to be performed under extremely clean conditions to prevent the surface from contaminating and oxidizing. Thus, the UHV environment is crucial for reliable STM investigations on clean surface of the sample. The system is equipped with one turbo molecular drag pump (Pfeiffer TMU261), two ion getter pumps (IGP) and one titanium sublimation pumps (TSP) whereas one SAES getter.

The UHV system of the LT-STM contains the STM chamber, PES chamber and the fast entry sample loadlock (FEL) chamber, each of which have their own specific functions. The FEL chamber is used to insert and extract tips and samples in and out of the vacuum. It is possible to make FEL chamber vacuum better than $1 \times 10^{-6} Pa$ for transfer the sample to PES chamber. In PES camber, samples can be cooled, heated and cleaved, LEED can be done on cleaned surfaces of samples and samples can be sputtered with Ar gas or deposited with evaporators. The STM chamber contains the STM stage, the vibration isolation elements and the cryogenic equipment. The STM head is optically accessible via a small viewport. The STM stage includes the sample plate, the probe tip, the scanner and the piezo motor. The samples or tip can be transferred to the STM stage by the wobble stick and the measurement will be processed here. In order to exchange the tip, we unfortunately have to unload the sample. This is a disadvantage of the Omicron LT-STM. The tip is manually positioned above the sample by piezo steppers while monitoring the position with a microscope attached to a charged coupled device (CCD) camera. The scanner, used for the fine movement of the tip during measurements, consists of a

single piezo tube. During measurements, the STM stage is hanging free, held vertically by the suspension springs and horizontally by the air damping. The cryogenic equipment consists of two to get concentric bath cryostats which allow one low temperature. The outer one is usually filled with liquid nitrogen and the inner one with either liquid nitrogen or liquid helium for the measurements at 77 K and 4.5 K respectively. The STM is mounted in two copper cups that are attached below and in thermal contact with the cryostats. The inner cup and the outer cup are screwed to the liquid helium cryostat and the liquid nitrogen cryostat, respectively. Both copper cups have three windows for optical access, and one window for changing sample plates and probe tips.

4.1.2 Tip preparation

There are several important factors for producing reasonable results in STM in UHV such as the construction of the STM, the quality of vacuum, sample and the probing tip. When performing STM/STS measurements, the stability of the tip plays a crucial role for collecting the tunneling current. The properties of the probing tip are reflected in the quality of the obtained data. Therefore, a sharp tip which comes to a point rapidly is desired. The super sharp tunneling tip should be made from a material that does not chemically interact and should also be rigid to ensure that there is the least reaction to movements in the STM. Tungsten is a very tough material which has the highest melting point with 3695 K and the highest tensile strength of all pure metals [63]. Tips made from W are therefore very stable over a wide temperature range and might even survive from a tip crash. The reliable preparation of tunneling tips is the most important point, but is also the trickiest experimental aspects of STM. The tips used here are electro-chemically etched from polycrystalline tungsten wire, with a diameter of 300 µm. Figure 4.2 shows the setup for an electrochemical etching device for making tungsten tips. Surface of the tungsten wire was stained with oxidization

that should be flashed first. A piece of tungsten wire (anode) is placed in

Figure 4.2: Chemical etching tool (TM-59060 of JOEL) inset with tip procedure.

a holder filled with an electrolyte concentration of 1 mol/l potassium hydroxide, the platinum ring acts as a counter electrode (cathode) as shown in the inset of Fig. 4.2. The DC voltage of 12 V creates a small current that travels in one simple loop. The current flows from the power supply to a pure salt water bath. Current then flows to the Pt loop and circuit is closed at the negative input of the power supply [64]. The overall chemical reaction at anode is:

$$W + 8OH^- \rightarrow WO_4^{2-} + 4H_2O + 6e^-, \quad (4.1)$$

While the cathode:

$$6H_2O + 6e^- \rightarrow 3H_2 \uparrow + 6OH^-, \quad (4.2)$$

Total Reaction:

$$\mathrm{w} + 2OH^- + 2H_2O \rightarrow WO_4^{2-} + 3H_2 \uparrow, \quad (4.3)$$

During the etching process, a concentration gradient of OH^- from the top of the meniscus to the bottom is created. Since the reaction product, WO_4^{2-} drops downward after creation, a second gradient of OH^- is created. The strongest etching thus takes place at the bottom of the meniscus, where the tungsten wire is formed into an hourglass shape. When the wire gets too thin it will break and two sharp tips are produced. To prevent blunting of the formed tip, the etching reaction should be stopped the moment the wire breaks. The etching power supply automatically terminates the etching process as soon as the current drops below a pre-set threshold value. The etching process takes $10\sim11$ min until a sharp tip is created. After drop-off, the tip is taken out of the solution and carefully rinsed in distilled water, in order to remove remainders of the etchant. After that we checked it by optical microscope or SEM, Fig. 4.3 shows the successfully etched tip image used in this work.

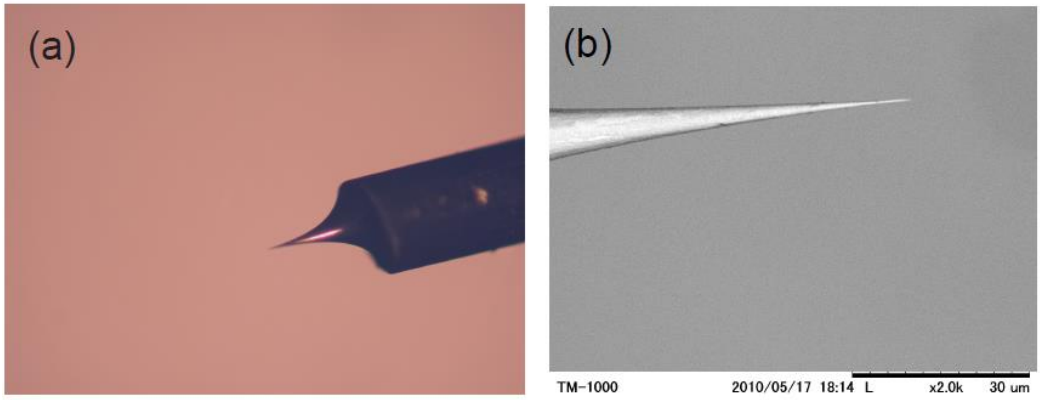

Figure 4.3: Successfully etched tungsten tip. (a) Visualizations under an optical microscope and (b) scanning electron microscope.

4.1.3 Tip annealing

Electrochemical etching yields tips which are microscopically sharp, but the down side it, a thick insulating layer is evolving during the etching procedure [65-68]. The tungsten surface contamination comes mainly from tungsten trioxide WO_3, as well as carbon, KOH conglomerates and $WO_3 - K$ microcrystals [69]. The important thing is

to get rid of any contaminants which may disturb tunneling. Various techniques have been suggested to remove these additional tunneling barriers to get sharpen tips. The *in situ* treatment is to direct anneal the tip is used here. The direct annealing method is relatively easy to perform. For direct heating, the tip carrier is brought into the tip holder to mechanical contact with a tungsten filament very carefully. A piece of 0.3 mm tungsten wire used as a filament inside the tip holder is heated by means of a standard direct current power supply in vacuum. Tip will be heated till the color turns into bright orange. Water and other solvents are removed at relatively low temperatures already. At approximately 1000 K the WO_3 layer will react with pure tungsten to form WO_2 which will sublimate:

$$2WO_3 + W \rightarrow 3WO_2 \uparrow, \tag{4.4}$$

The tungsten dioxide is volatile. As the WO_3 layer is removed from the tip, a pure tungsten surface is generated.

A disadvantage, however, is that the process is difficult to control. The whole tip shank is being heated up, and the exact heat flowing to the apex cannot exactly be predicted. Tip may accidently be molten if heated too strongly. Due to the high melting point (3410 ℃) of tungsten, the tip itself will not be affected. However, elevated temperatures also enhance the diffusion of surface atoms. This can lead to blunting of the tip below the melting point [65]. Hence, it is necessary to protect the tips from being overheated. When bringing the tip into contact with the filament, one can easily bend or crash the tip. By applying to much force, one might even break the filament since tungsten becomes brittle once it had been annealed. Nonetheless, if carried out carefully, this direct heating procedure is useful as a first gentle treatment step or in connection with other methods.

4.1.4 Characterization of tips on Si (111) surface

Once an etched tip has been treated to remove oxides, it has to be characterized on a known surface before an actual measurement is performed on an unknown material. To test the quality of tips in STM we have imaged a 7×7 reconstruction of Si (111) surface, which is well-known to firstly exhibit the resolving power. The sample was placed in the STM stage after we get the clean surface of Si (111) 7×7 structure by direct heated at 1250K. The chamber was kept at a pressure of $1 \times 10^{-9}\ Pa$ and 78 K for measurement. In order to further modify or to sharpen the tip, by applying voltage pulses up to $(1\sim10)$ V between tip and sample a high electric field at the tip apex has been generated.

The quality and resolution of the STM image is dependent completely on the shape of the tip. Fig. 4.4(a) presents a typical topography images and its $\mathrm{dI/dV}$ maps on clean surface of Si (111) taken at 78 K. The STM images of Si(111)7×7 reveal 12 protrusions in each unit cell, and the negative biased STM image clearly shows the inequivalence between the adatoms in the two halves of a unit cell. Besides, there is a corner hole in each unit cell. The information immediately helps to rule out many

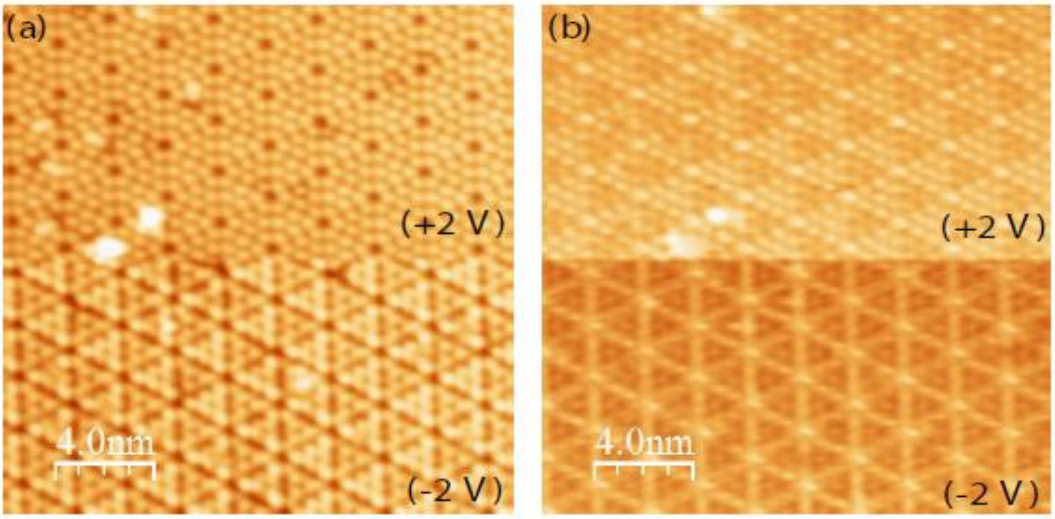

Figure 4.4: (a) The STM topography taken in both empty and filled states of Si (111) clean surface and its dI/dV images (b).

models proposed at that time.

Besides studying the topography of a surface, STM allows to obtain spectroscopic information with atomic resolution [43]. Therefore, a measurement of $\mathrm{dI/dV}$ as a function of sample bias V allows in principle to measure the sample LDOS in a given energy range close to the Fermi energy. In order to acquire a tunneling spectrum, the tip is placed at a single point or over a point of interest (x, y) on the sample surface. Then the feedback loop is opened, and z determined by the set point current remains constant, while the bias voltage $\mathrm{V_s}$ is ramped and the tunneling current $I(V)$ is recorded. The situation is however complicated by the fact that the tunneling

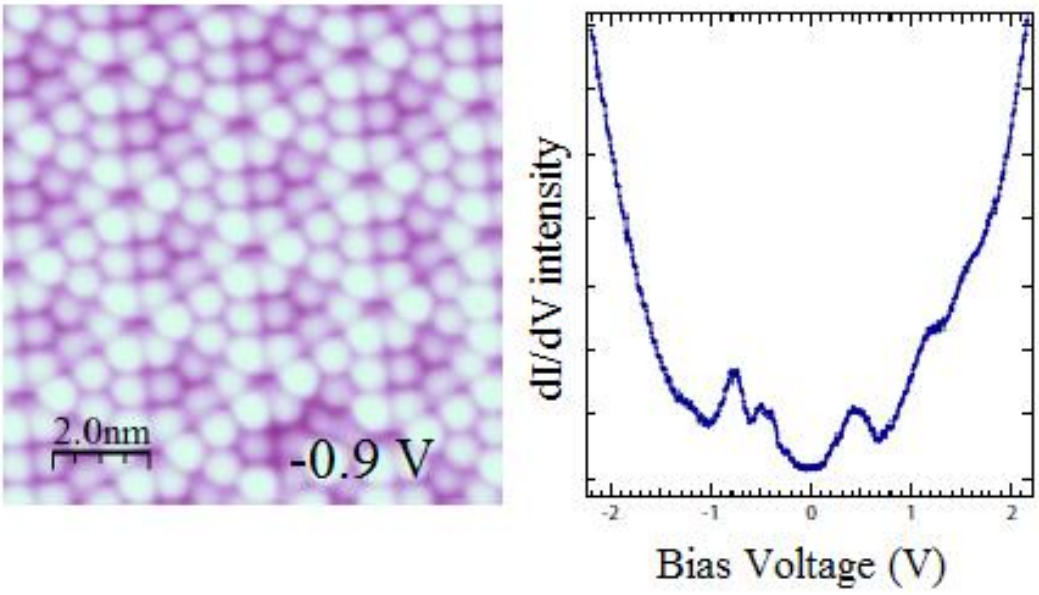

Figure 4.5: (a) The STM topography of Si (111) clean surface at -0.9 V and (b) the STS spectrum

transmission probability is bias dependent. This non-constant contribution of the tunneling transmission probability to a dI/dV spectrum can be corrected to some extend by an appropriate normalization procedure. As is characteristic for semiconductor we observe a large gap in the LDOS ranging from roughly $-1\ \mathrm{V}\sim 1\ \mathrm{V}$.

4.2 ARPES setup

ARPES experiments were conducted using the synchrotron radiation at beamline 7 (BL-7) equipped with a hemispherical photo-electron analyzer (VG-SCIENTA SES2002) of Hiroshima Synchrotron Radiation Center, which usually named as Hisor. The synchrotron radiation is emitted from a compact 750 MeV electron storage ring with a 2.7 T polarized electromagnet. The critical wavelength is 1.42 nm. Hisor was designed for race-truck-type storage ring and its circumference is 21.95 m. Linear and helical undulators are installed at the two straight sections as an insertion device [31, 32]. The electron beam-current is currently 300 mA for the initial injection, and the electron-beam lifetime is longer than 10h. Figure 4.6 shows a schematic design of the Hisor. There are 14 beamlines in Hisor and 11 of them utilizes the radiation emitted from the bending magnet parts.

A Dragon-type grazing incidence monochromator, has been installed at bending magnet beamline, BL-7. This beamline assumes to perform experiments, which

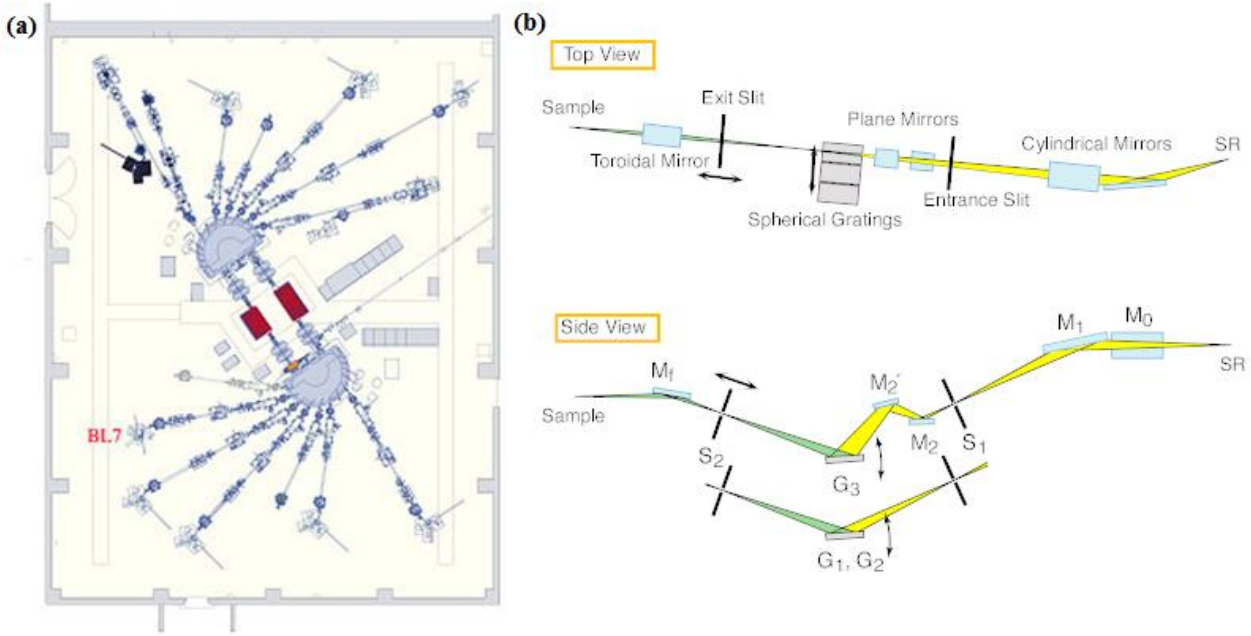

Figure 4.6: (a) Arrangement of experiment hall. BL7 is placed at end of bending magnet section of Hisor ring. (b) The schematic layout of the BL-7 in the top and side view.

makes the most of merit of bending magnet section of wavelength tunability. Figure 4.6(b) shows the schematic optical layout of the beamline. This beamline is consists of the cylindrical mirrors (M_0, M_1), toroidal mirror (M_t), plane mirrors (M_2, M_2'), an entrance slit (S_1), spherical gratings (G_1, G_2, G_3), an exit slit (S_2). They are connected by the cylindrical ducts and kept under an ultra-high vacuum $10^{-8}\ Pa$. The spherical gratings are available, and can be exchanged in vacuum.

The end station of the beamline BL-7 is composed by an analyzer chamber and sample preparation chambers. The setup is shown in Fig. 4.7. The analyzer chamber is equipped with a SES2002 electron energy analyzer and MCP detector for electron field measurement. The preparation chamber is equipped with LEED, ion sputtering guns, gas- inlet system and several optional ports for sample preparation accessories.

Figure 4.7: BL-7 experimental system. PES spectrometer is equipped with a He cryostat for low temperature experiment. The sample preparation chamber has components of sample cleaning for bulk or surface experiments.

When monochromatized synchrotron radiation is incident on a material, the photoelectron is emitted in the UHV main chamber. It enters the electro-optical lens in front of the analyzer entrance slit and are focused parallel electron beams by

electrostatic fields. After passing through the electrostatic fields between the outer and inner concentric hemispheres, the electrons reach a two dimensional multi-channel plate (MCP) detector as a signal. This detection system is based on a MCP detector monitored and counted by CCD camera. The two dimensional detector creates an image with one axis representing angle and the other kinetic energy in real time on the computer screen.

5 Direct observation of spin filtered surface state scattering in the Bi_2Te_2Se

Interband optical excitation of topological surface states by pulsed laser light is expected to generate longer lived spin-polarized carriers at the surface [9, 10]. To understand the photo-excited spin and charge dynamics, knowledge of unoccupied topological surface state far above the Dirac point and the unoccupied bulk continuum is crucial. Note that photoelectron spectroscopy, with which most of the studies on topological insulators have been performed, cannot access unoccupied states or provide direct information on the in-plane electron scattering. Thus, there has been a dearth of measurements on the unoccupied electronic states of 3D TIs, and the present study is motivated by the necessity of getting the information about the unoccupied spectrum.

Here, a quasiparticle interference pattern due to surface scattering is revealed on Bi_2Te_2Se with a low-temperature STM experiment in combination with the first-principles calculation and the model calculation using $k.p$ Hamiltonian over a wide sample bias (energy) range. Meanwhile, the surface energy band structure is determined by employing $k.p$ theory, used to explain the experimental data. A strong warping of CECs of the TSS explains the anisotropic spin-filtered scattering, which persists into the unoccupied state region, where the surface state coexists with bulk conduction band. This chapter is mainly adopted from our published results in reference [69].

5.1 Electronic structure of Bi_2Te_2Se

Scanning tunneling microscopy (STM)/ spectroscopy (STS) has been widely used to study the surfaces of 3D TIs as one of the most surface sensitive techniques providing direct information on the electronic structure of topological surface states

and their scattering properties. One can unveil the spin structure of surface states through the presence or absence of standing waves both for occupied and unoccupied states. Fourier transformed images of the observed standing waves give bias-dependent scattering vectors in momentum space. For an isotropic TSS, the backscattering is strongly suppressed, while a spin conserving scattering is allowed, and it has actually been observed in several topological insulators with warped constant energy contours (CECs) [70–77]. A non-spin-conserving scattering can also occur if the time reversal symmetry is broken, i.e., in the presence of magnetic impurities [78].

Our experiments were performed using an LT-STM (Omicron NanoTechnology GmbH) operated at 4.5 K in ultrahigh vacuum. Bi_2Te_2Se crystal was grown by modified vertical Bridgman method as described elsewhere [79]. With our STM, we have examined several Bi_2Te_2Se crystals, grown under the same conditions, and we have not noticed any sample dependence for any of the results we present. A chemically etched tungsten wire was used as an STM tip, and the quality of the tip apex was examined by scanning an atomically clean Si (111) surface. The STM images were obtained in a constant- current mode, and the differential conductance dI/dV maps were measured simultaneously with recording the STM images using a standard lock-in technique. ARPES experiments were conducted using the synchrotron radiation at BL-7 equipped with a hemispherical photoelectron analyzer (VG-SCIENTA SES2002) of Hiroshima Synchrotron Radiation Center (HSRC). Samples were cleaved in ultra-high vacuum in situ at room temperature for the STM and at 10-20 K for ARPES measurement.

5.1.1 Visulazing defects on the surface of Bi_2Te_2Se

The defects and impurities in 3D TIs dramatically dominate its thermoelectric and topological properties. There have been several existing literatures dealing with the defects in Bi_2Te_3 and Bi_2Se_3 which could dramatically influence on the surface states

of these materials. Here we discuss about the defects on the surface of Bi_2Te_2Se.

Bi_2Te_2Se has an ordered tetradymite structure, derived from Bi_2Te_3 by replacing the central Te layer with a Se layer. Since here the Se atoms are confined in the central layer the formation of Se vacancies and the anti-site defects between Bi and Te atoms is expected to be less probable [60], which would suppress the bulk conductivity. Similar to Bi_2Se_3 and Bi_2Te_3, Bi_2Te_2Se forms a rhombohedral crystal structure with the space group $D_{3d}^5(R\bar{3}m)$, with the basis quintuple layer (QL) unit of Te-Bi-Se-Bi-Te, as depicted in Fig. 5.1(a). Inside the QL the bonds are predominantly ionic-

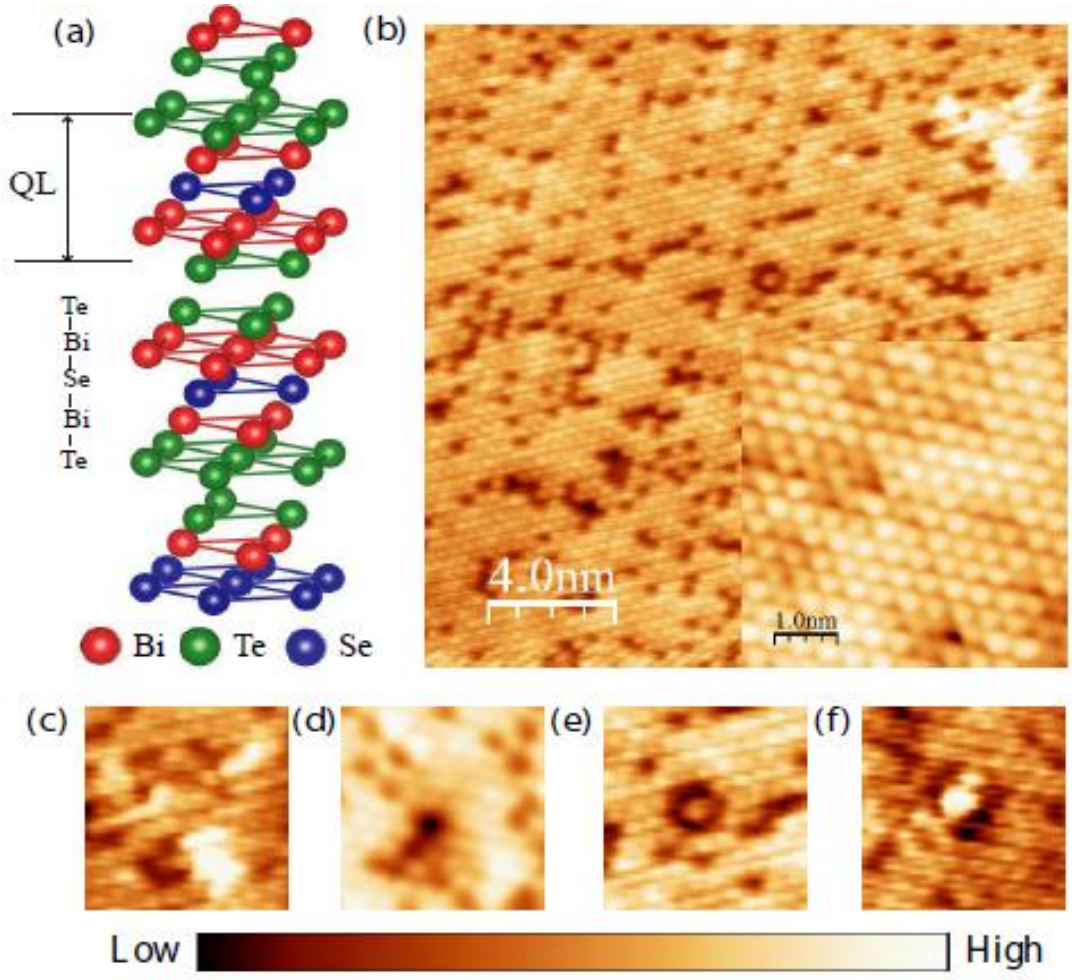

Figure 5.1: (a) Crystal structure showing three quintuple units of Bi_2Te_2Se. (b) The STM topographic image (45 nm×45 nm) on cleaved surface of Bi_2Te_2Se at -400 mV inset with atomic-resolution image (5 nm×5 nm) obtained with bias voltage −50 mV. (c)- (f) Typical defects on the surface of Bi_2Te_2Se.

covalent, and adjacent QLs are bound by van der Waals forces. Fig. 5.1(b) shows the STM topographic image on the cleaved surface of Bi_2Te_2Se area of $20\ nm \times 20\ nm$ at a bias voltage of -400 mV. One can see in the image which mainly appears as a hole in both occupied and unoccupied state topographies, therefore signifying that it is electrically neutral and considered to be Se-Te antisite defect [80]. Inset is atomic-resolution image $(-50\ \text{mV}, 0.12\ \text{nA})$ acquired in the area of $5\ \text{nm} \times 5\ \text{nm}$, demonstrating a six-fold symmetry of Te atoms in the topmost layer, where each bright spot corresponds to a single Te atom. There are several types of defects except for Se-Te antisite defect as shown in Figs. 5.1(c)-5.1(f). Defect (c) is triangular, also imaged in Bi_2Te_3 and Bi_2Se_3 with an edge length of two atoms, centered directly between lattice sites in the upper Te layer. It thus resides in the Bi layer just below the upper Te layer. This defect is identified as either a Te or a Se antisite defect on the Bi layer. Defects (d)-(e) correspond to Te or Se antisite defects located on Bi layer. Defect (f) appears as high circular hump with very small amount in the image and identified as adatoms remnant from the cleavage process [80]. We discuss how these defects affect the topological nature of this compound in the following section.

5.1.2 The LDOS measurement of Bi_2Te_2Se

The scanning tunneling spectrum gives a measure of the local density of states near the Fermi energy as shown in Fig. 5.2(a). The resulting STS data were averaged over 10 spectra to improve statistics. The dashed lines show approximate energy locations of the top of the bulk valence band (BVB), Dirac point (DP) and the bottom of bulk conduction band (BCB) around the $\bar{\Gamma}$ point. Figure 5.2(b) depicts the surface state energy dispersion of Bi_2Te_2Se measured by ARPES at a photon energy of $h\nu = 30$ eV [open circles indicate the band dispersion by our ab initio calculation [see Fig. 5.9(a)] shifted downward by 0.24 eV to match the measured Dirac point position]. The DP energies from ARPES and STS spectra are identical [80]. Although the

tunneling spectroscopy measurement gives information about LDOS near the Fermi energy, but it does not distinguish between bulk and surface states, and a different approach is needed to solely probe the surface states.

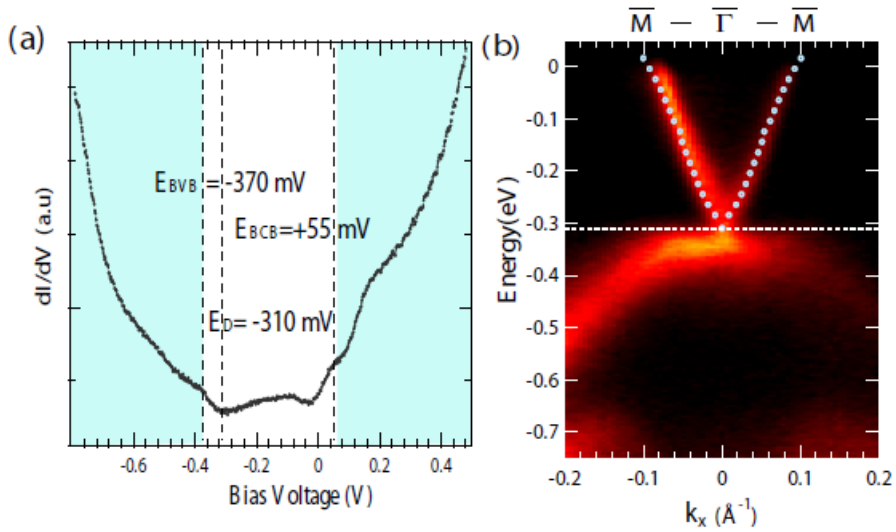

Figure 5.2: (a) Averaged STS spectrum indicating the approximate position for Dirac point (E_{DP}), bulk valence band (E_{BVB}) and bulk conduction band (E_{BCB}), respectively. (b) Energy-momentum ARPES intensity distribution map along the $\bar{\Gamma}\bar{M}$ direction acquired with a photon energy of 30 eV (Taken from [69]).

5. 2 Imaging qusiparticle interference in Bi_2Te_2Se

Quasiparticle interference patterns measured by scanning tunneling microscopy can be used to study the local electronic structure of novel materials. Probing the interaction of quasiparticles with impurities and defects has proven to be a powerful tool for the study of electronic structure in solids. Standing waves caused by scattering off from crystal defects or point like impurities on the surface of 3D TIs is an effective way to reveal the topological nature of the surface states. The interference between incoming and outgoing waves at specific momenta leads to an oscillation in the local density of state (LDOS). Nowadays, such modulation can be studied by one more powerful surface probe, scanning tunneling microscopy (STM), directly in real

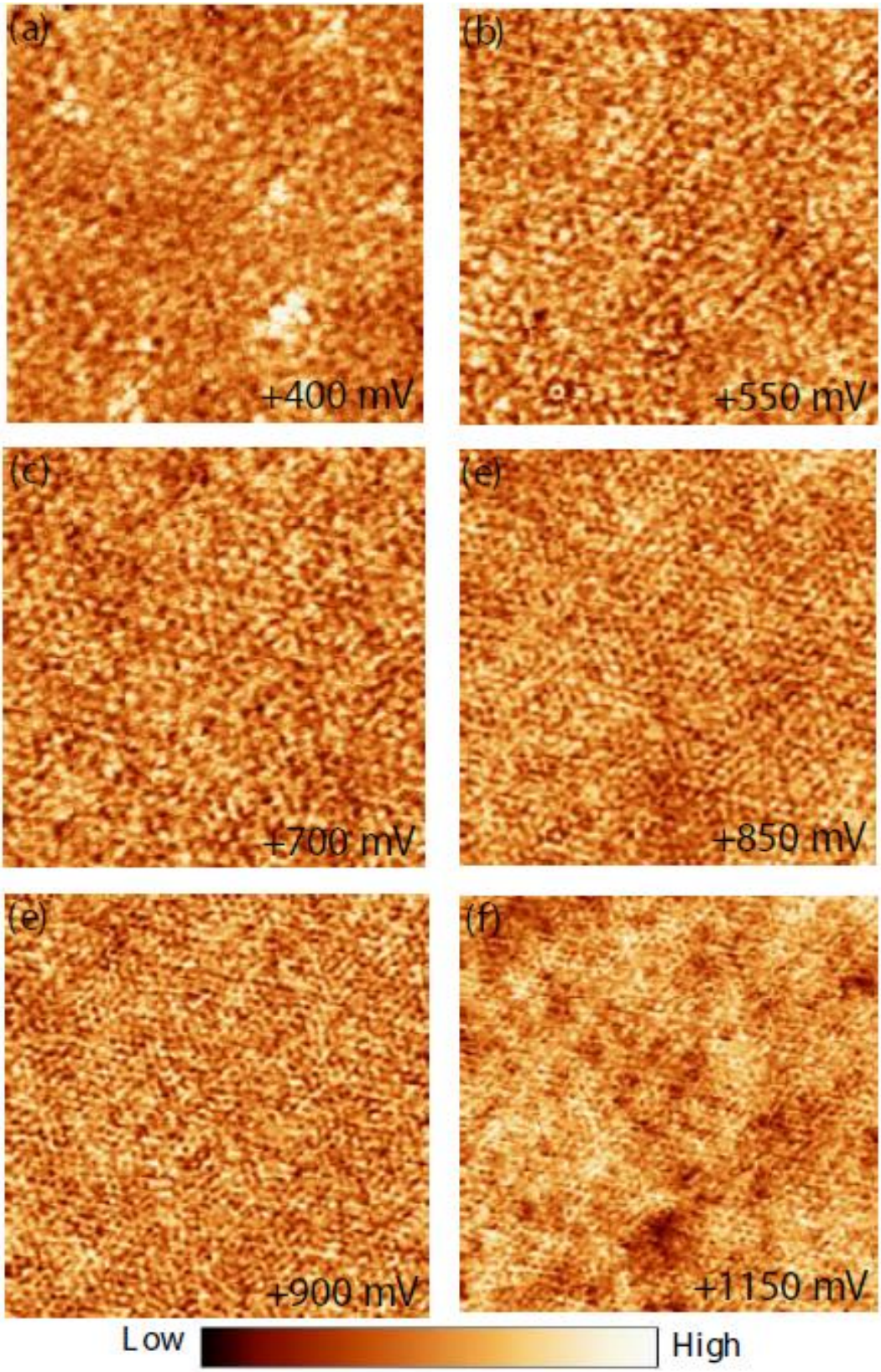

Figure 5.3: (a)-(d) Differential conductance map (dI/dV map) of Bi_2Te_2Se surface at 4.5 K with various sample bias voltage in the 45 nm×45 nm area (set point $I = 0.15$ nA).

space and provide information in momentum space through Fourier transformation of real space images. This is potentially a powerful technique because, for any energy, it simultaneously yields real-space and momentum-space information on the wave functions, scattering processes, and dispersion of the quasiparticles.

Figures 5.3(a) - 5.3(d) shows the differential conductance (dI/dV) map at various bias voltage. It exhibits a standing wave spreading anisotropically around point defects. All the spectroscopic maps at the bias voltages from +50 to +1250 mV were obtained for the same surface without changing any other experimental parameters. Notably, different spatial patterns and wavelengths are observed at different energy. The wavelength decreases as the bias voltage goes away from the Dirac point and is determined by the momentum transfer during scattering at a given energy [70]. The superposition of waves with various wavelength smears out the interference patterns. Although the existence of standing waves has been previously reported in STM studies of Bi_2Te_3, but there is as yet no evidence of its persistence in higher energy region far beyond the Dirac point.

In order to get the momentum space information and obtain the scattering wave vectors, we have performed Fast Fourier Transformation (FFT) of the dI/dV maps, see Figs. 5.4(a)-5.4(l). These scattering images provide information on bias-dependent quasiparticle interferences which display the allowed scattering vectors and relative intensities during the scattering processes of the surface state electrons. One important feature in these images is that the high intensity is always oriented toward $\bar{\Gamma}\bar{M}$ direction while the intensity in the $\bar{\Gamma}\bar{K}$ direction vanishes. For bias voltages below +300 mV the interference effect around the point defects is weak, and the FFT image shows a circular pattern with small q vectors, which mainly come from the statistical noise. At $V_s = +400$ mV, flower shaped patterns emerge [Fig. 5.4(b)] with six broad petals along $\bar{\Gamma}\bar{M}$. Note that the pattern becomes sharp and intensive at bias voltages between $+550$ and $+850$ mV. Starting with $V_s = +950$ mV, with increasing the

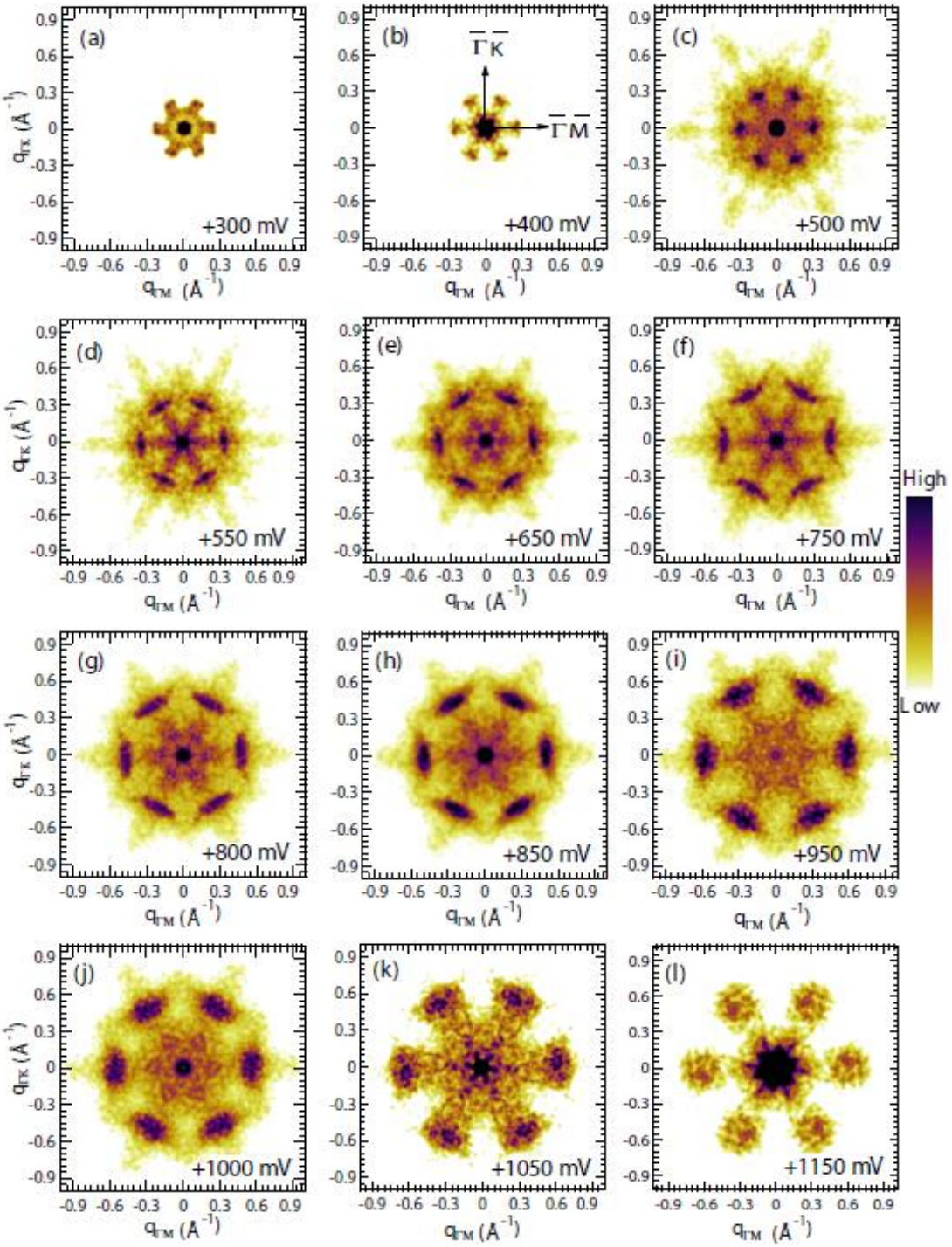

Figure 5.4: (a)-(l) Fast Fourier transformed images for several bias voltages showing six strong spots along the $\bar{\Gamma}\bar{M}$ direction. The FFT patterns are hexagonally symmetrized (Taken from [69]).

bias voltage the spots get gradually broader.

The evolution of the scattering vectors with V_s is visualized by the FFT power

profiles in Figs. 5.5(a) and 5.5(b). In Fig. 5.5(a), in the $\bar{\Gamma}\bar{M}$ direction (rightwards) the scattering vectors become larger as V_s increases, while there is practically no scattering along $\bar{\Gamma}\bar{K}$ (leftwards).

In Fig. 5.5(b) we show the ratio of the intensity profiles along $\bar{\Gamma}\bar{M}$ and $\bar{\Gamma}\bar{K}$. The intensities ratio damps the background and makes the scattering more clear: we distinctly see the dispersion of q with the bias voltage. The two linear dispersions can be extrapolated to the lower V_s and eventually they intersect at the Dirac point of -310 mV, which is again consistent with the ARPES result [Fig. 5.2(b)].

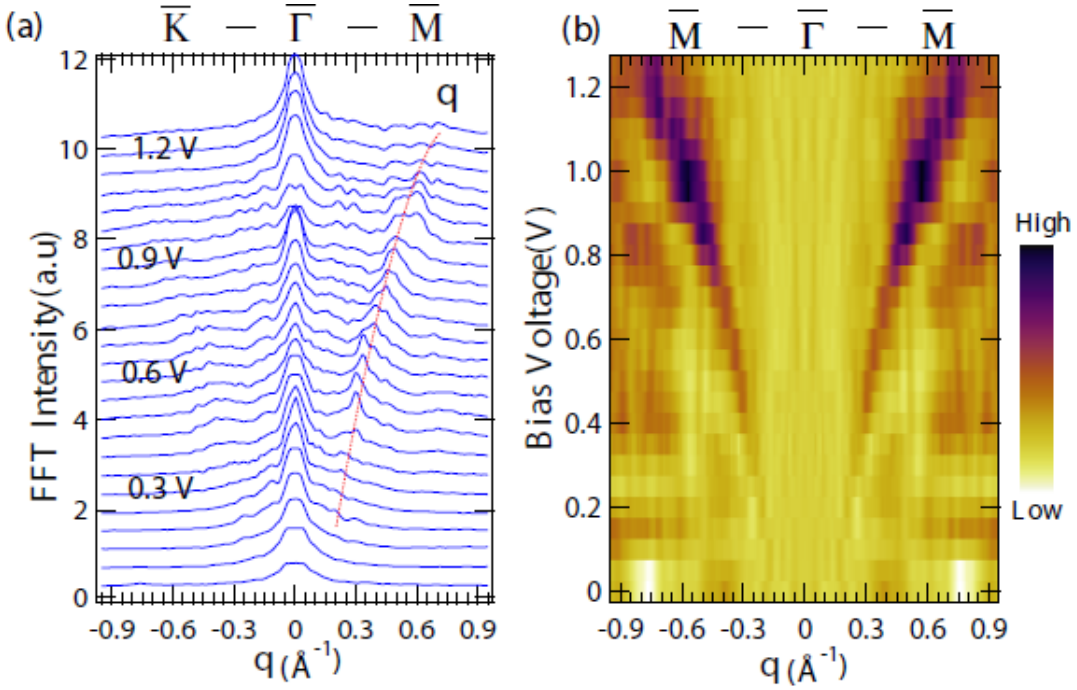

Figure 5.5: (a) FFT intensity profiles from $+0.05$ V to $+1.25$ V with a step of $+0.05$ V display the bias voltage dependent scattering along $\bar{\Gamma}\bar{M}$ (positive q) and $\bar{\Gamma}\bar{K}$ (negative q) directions. (b) The ratio of the FFT intensity profiles along $\bar{\Gamma}\bar{M}$ and $\bar{\Gamma}\bar{K}$ (Taken from [69]).

5.3 Hexagonally warped topological surface state of Bi_2Te_2Se

The previous section has yielded rich information about the quasiparticle interference structure on the surface of Bi_2Te_2Se. These bias-dependent quasiparticle scattering is characterized by scattering vectors that connect the k vectors of the initial

and final scattering states at the constant energy contour (CEC). The joint density of states (JDOS) has an inherent relationship with QPI patterns and can be independently determined from ARPES experiment. To include scattering of topological surface state electrons affected by bulk conduction band, the experimental results are compared with those obtained by the model calculation using the effective Hamiltonian:

$$H(\vec{k}) = {k^2}/{2m^*} + v(k_x\sigma_y - k_y\sigma_x) + {\lambda}/{2}\,(k_+^3 + k_-^3)\sigma_z \qquad (5.1)$$

where $k_\pm = k_x \pm ik_y$ and $(\sigma_x, \sigma_y, \sigma_z)$ is the Pauli matrix acting on spin space. Here, m^*, $v = v_k/(1+\alpha k^2)$, and λ denotes an effective mass, a Dirac velocity, and the warping parameter, respectively. Besides $\vec{k} = (k_x, k_y)$, and k_x , k_y are the momentum component along the along $\bar{\Gamma}\bar{M}$ and $\bar{\Gamma}\bar{K}$ directions of the surface Brillouin zone, respectively. The energy eigenvalues of Hamiltonian are:

$$\varepsilon_\pm(\vec{k}) = {k^2}/{2m^*} \pm \sqrt{(v_k k)^2 + \lambda^2 k^2 cos^2(3\theta)}, \qquad (5.2)$$

here + (−) stands for conduction (valence) band and θ is the azimuth angle of momentum $\vec{k}$.

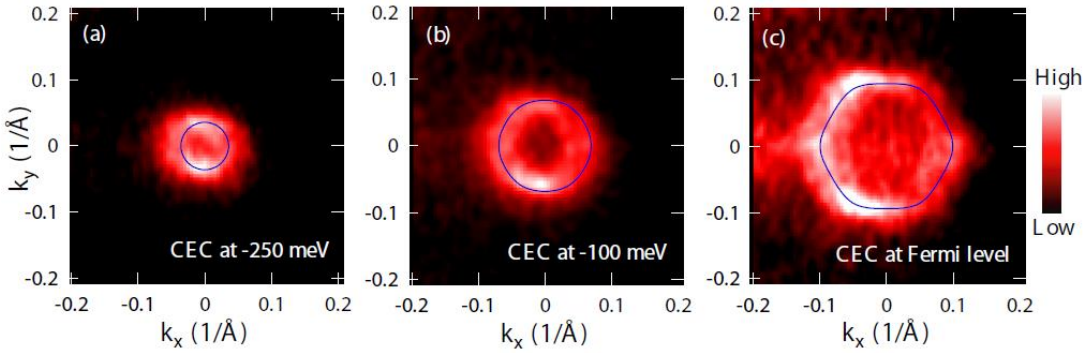

Figure 5.6: (a-c) Fermi surface contours of the surface state at different energies.

The parameters are chosen as $m^* = 0.36\ m_e$, $\alpha = 2.31\ Å^2$, $v_k = 2.41\ eV$ Å and

$\lambda = 126eV$ Å^3, to get a sufficient match with the ARPES results. The CECs of the surface state from the ARPES results were compared with the calculated ones by $k.p$ theory. One can see in Figs. 5.6(a)-5.6(c) that the calculated CECs adequately reproduce the experimental results and display the transition of Fermi surface from circular to hexagon shape.

As mentioned in chapter 3, JDOS can be described as a function of the momentum difference between initial and final scattering states, $\vec{q}$, using,

$$JDOS(\vec{q}) = \int I(\vec{k})\, I(\vec{k}+\vec{q}) d^2\vec{k}, \tag{5.3}$$

where $I(\vec{k})$ is the ARPES intensity that is proportional to the surface states' density of surface states at a specific 2D momentum $\vec{k}$. To calculate FFT patterns, we use the spin-dependent scattering possibility (SSP):

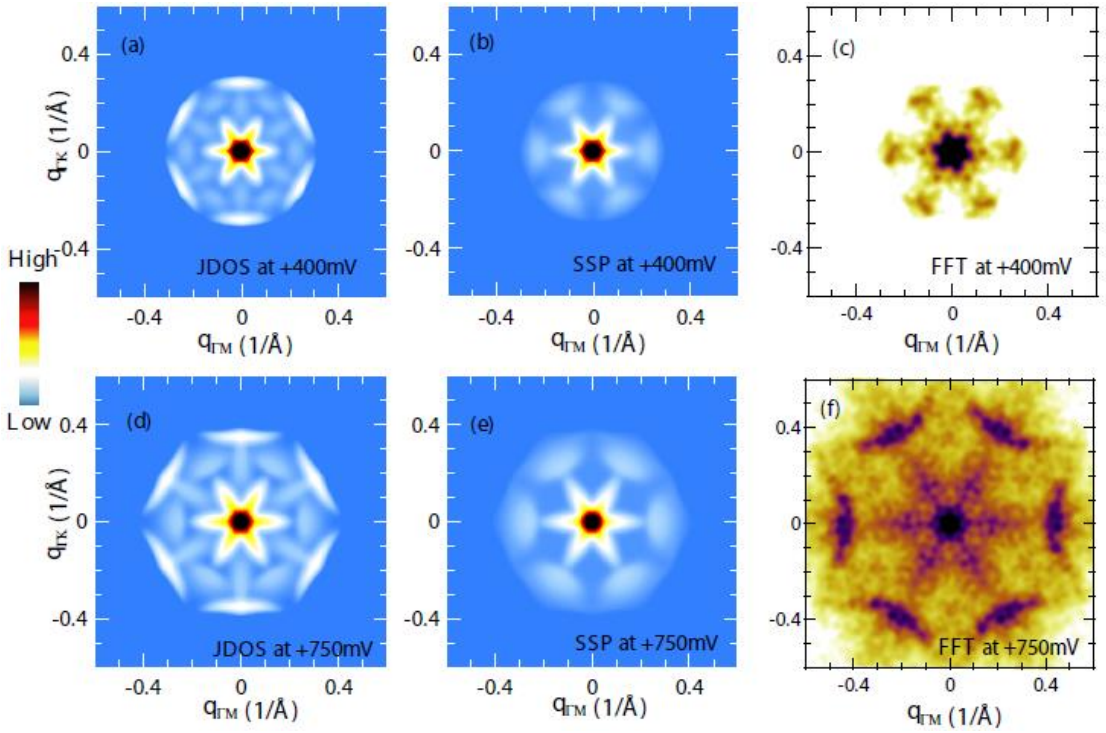

Figure 5.7: (a)–(f) The comparison of the FFT interference pattern with [(b) and (e)] and without [(a) and (d)] spin polarization calculated with $k.p$ theory and present work [(c) and (f)] at bias voltage of $+400$ mV and $+750$ mV, respectively. The $\bar{\Gamma}\bar{M}$ direction corresponds to x-axis.

$$SSP(\vec{q}) = \int I(\vec{k})\, T(\vec{q},\vec{k}) I(\vec{k}+\vec{q}) d^2\vec{k}, \tag{5.4}$$

here $T(\vec{q},\vec{k})$ is scattering matrix element.

The calculated JDOS without any spin filtered effect [Figs. 5.7(a)-5.7(d)] and the SSP [Figs. 5.7(b)-5.7(e)] were compared with the present result [Figs. 5.7(c)-5.7(f)] for $+400$ mV and $+750$ mV, respectively [72, 78].

The scattering patterns of JDOS in Figs. 5.7(a) and 5.7(d) are quite complex. There are six-broad intensities with rather high q values along the $\bar{\Gamma}\bar{K}$ direction in addition to the flower shaped pattern with smaller q values extending along the $\bar{\Gamma}\bar{M}$ direction. Weak intensities are also recognized for both $\bar{\Gamma}\bar{M}$ and $\bar{\Gamma}\bar{K}$ directions. Once the spin-filtered scattering is considered, all the scattering intensities along the $\bar{\Gamma}\bar{K}$ direction are diminished and only those along the $\bar{\Gamma}\bar{M}$ remain as shown in Figs. 5.7(b) and 5.7(d). Note that the spin- filtered quasiparticle interference images [Figs. 5.7(b) and 5.7(d)] are similar to the experimental result [Figs. 5.7(c) and 5.7(f)]. With the exception of the scattering vector size, from both figures we can see the flower shaped pattern and six broad intensities along the $\bar{\Gamma}\bar{M}$ direction while the scattering feature along the $\bar{\Gamma}\bar{K}$ is absent. The scattering vector size in the experiment is almost twice as large as the calculated one at $+750$ mV, while there is a good corresponds between them at $+400$ mV.

To clarify the relation between experimental and theoretical results, the intensity maxima of the FFT power profiles is plotted in the right panel of Fig. 5.5(a) and compared with the $|q|$ values extracted from the $k.p$ model Hamiltonian shown in Fig. 5.8. The inset shows a schematic CEC calculated by $k.p$ theory and model CEC estimated with the present result at $V_s = +750$ mV, respectively. Of the two, the latter displays a strong hexagonal warping of CEC than the former. The scattering channels open up due to an emergence of out-of-plain spin components at high energy and connected by simple nesting vectors q (black arrow) on the CEC. There should be

another scattering contribution ranging from 0 to q, which can result in the continuous internal flower shaped pattern extending along $\bar{\Gamma}\bar{M}$ direction.

Below $V_s = +400$ mV, the position of intensity maximum in Fig. 5.8 fits very well with those obtained by the scattering vector q from the model calculation. Above $+400$ mV, however, the experimental intensity maximum deviates significantly from the calculated q and disperses to much higher q values. This could originate from the larger CECs compared to those derived from $k.p$ theory. On another aspect, above

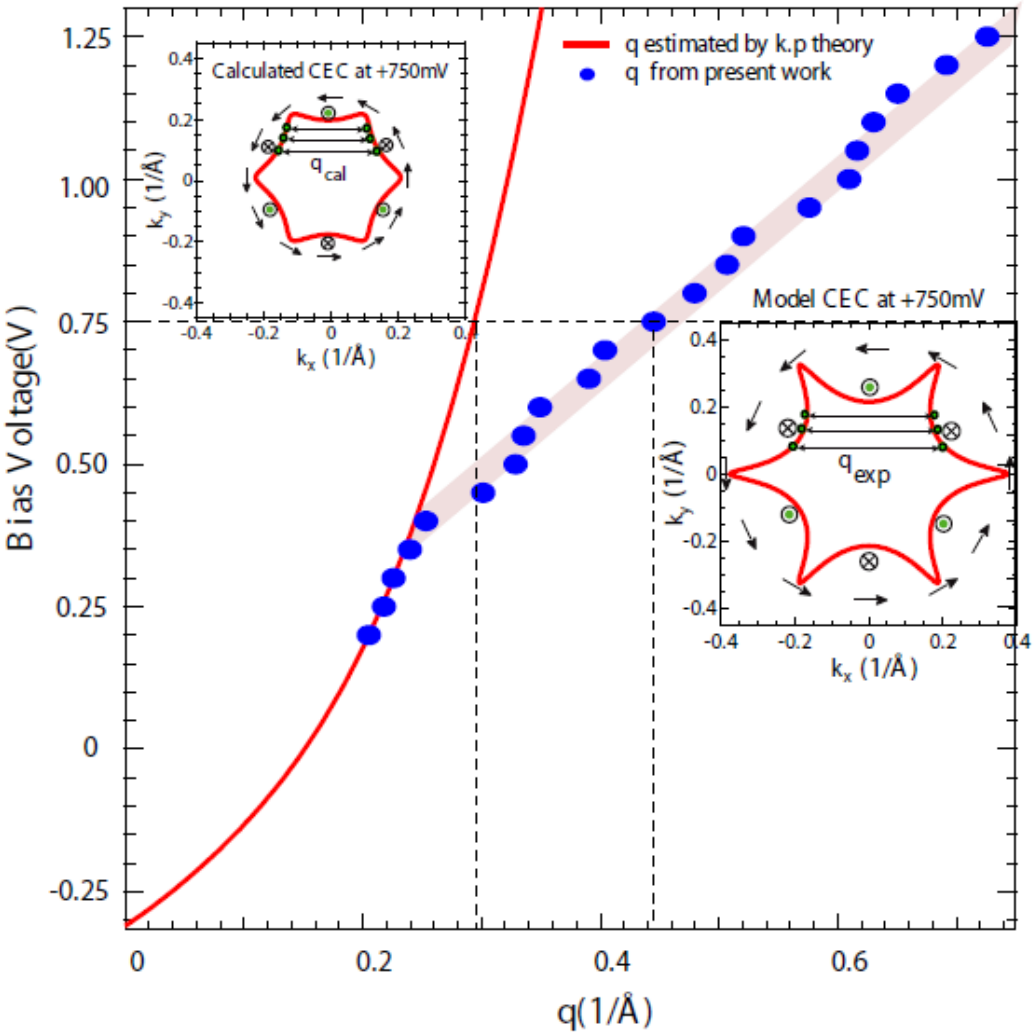

Figure 5.8: Dispersion of scattering vectors from STM and $k.p$ theory inset show schematic and model constant energy contours.

+400 mV, the band dispersion of this system may be influenced by bulk conduction band.

Apart from the mismatch between the experimental scattering vectors and those extracted from the $k.p$ model Hamiltonian, the appearance and the absence of FFT intensities along the $\bar{\Gamma}\bar{M}$ and $\bar{\Gamma}\bar{K}$ directions tells us that the scattering is spin filtered due to the strong warping of CECs. This would provide higher-energy electronic structure at the surface of Bi_2Te_2Se serving as a vital complement of ARPES measurement.

5.4 Ab initio studies on Bi_2Te_2Se

However, $k.p$ model Hamiltonian calculations are quite limited due to the large system size. In order to study both the bulk and the surface behaviors simultaneously, which is necessary to identify its topological nature, a large slab-type supercell is needed, and demanding calculations are involved. Topological nature and the surface states of Bi_2Te_2Se in unoccupied state have been studied by *ab initio* calculations.

In order to further elucidate the origin of scattering pattern and the effect of the helical spin texture of the TSS, we have performed a first-principles calculation of the electronic structure of a 7 formula units slab of Bi_2Te_2Se [81]. Figure 5.9(a) shows the band structure along $\bar{\Gamma}\bar{K}$ (leftwards) and $\bar{\Gamma}\bar{M}$ (rightwards). The magenta arrows show the energy and momentum ranges of the TSS, and the green arrows indicate the range of the inner surface state (ISS), which splits off from the top of the conduction band. Here, the DP is localized 0.065 eV below the calculated Fermi energy, i.e., the experimental energy scale is shifted by 0.24 eV relative to the theoretical scale [see Fig. 5.2(b)].

Figures 5.9(b) and 5.9(c) show the depth-momentum distribution (in the $\bar{\Gamma}\bar{K}$ direction) of the charge density $\rho(z, k_{\parallel})$ for the upper-cone TSS [Fig. 5.9(b)] and for the ISS [Fig. 5.9(c)]. The upper-cone surface state exists up to $k_{\parallel} = 0.22$ Å^{-1}, and

the ISS between 0.08 and 0.2 $Å^{-1}$.

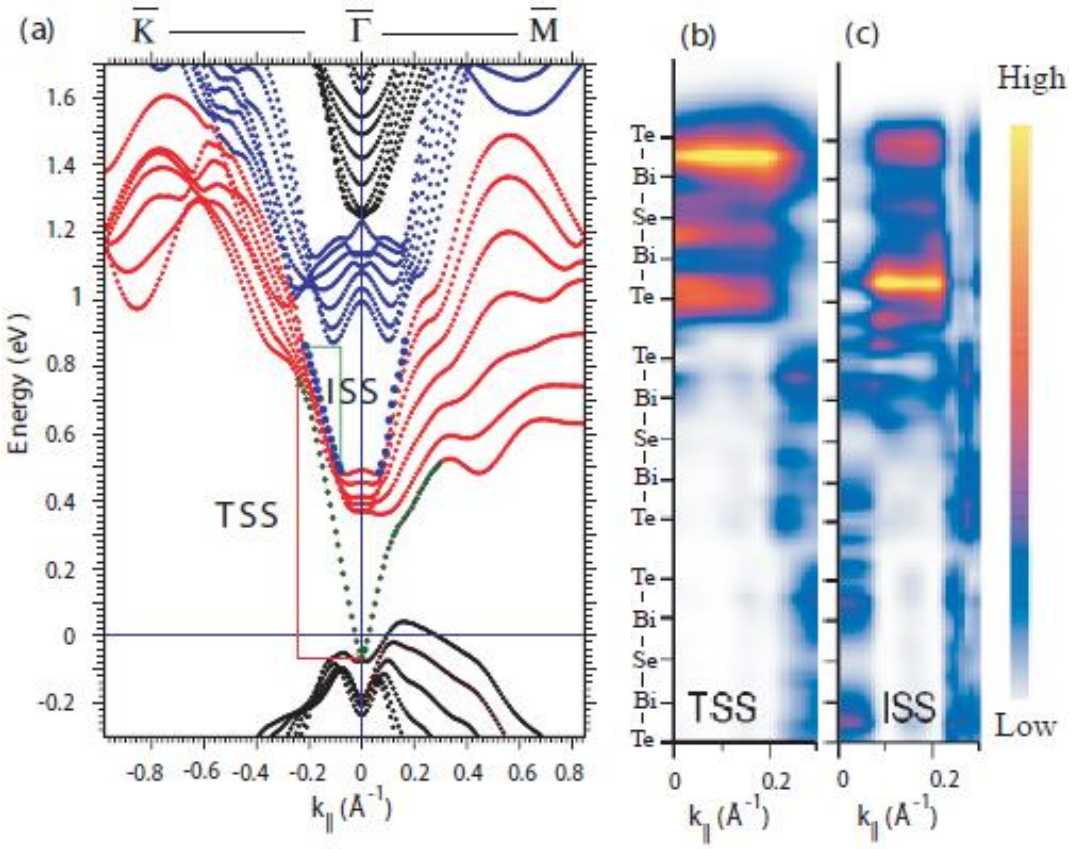

Figure 5.9: (a) First principles electronic structure of a 7 formula units slab of Bi_2Te_2Se. (b)-(c) The depth-momentum distribution of the charge density for topological surface state (TSS) and inner surface state (ISS). In view of the finite thickness of the slab shown is the sum of the densities of the degenerate pair of the surface states located on the opposite surfaces of the slab (Taken from [69]).

Calculated momentum distributions of the spatially-resolved spectral density $N(E, k_{\|})$ with several constant energies were shown in Figs. 5.10(a)–5.10(C). Evolutions of the "surface-related" Fermi surfaces with energy range from $(440 \sim 760)$ meV above the Fermi energy. The ISS starts from 500meV above the Fermi energy where only TSS acts a role in Figs. 5.10(a). As we all can see the TSS strongly localized at these energies influenced by bulk conduction band. The function is defined as a sum over all (discrete) states λ with energy E and Bloch vector $k_{\|}$

weighted with the probability $Q_{\lambda k_\parallel}$ of finding the electron in this state in the surface region:

$$N(E, k_\parallel) = \sum_\lambda Q_{\lambda k_\parallel} \delta(E_{\lambda k_\parallel} - E), \tag{5.5}$$

For the sake of presentation, the δ function is replaced by a Gaussian of 0.05 eV full width at half maximum. The integral

$$Q_{\lambda k_\parallel} = \int \left|\psi_{\lambda k_\parallel}(r)\right|^2 dr, \tag{5.6}$$

over the surface region comprises two outermost atomic layers and vacuum.

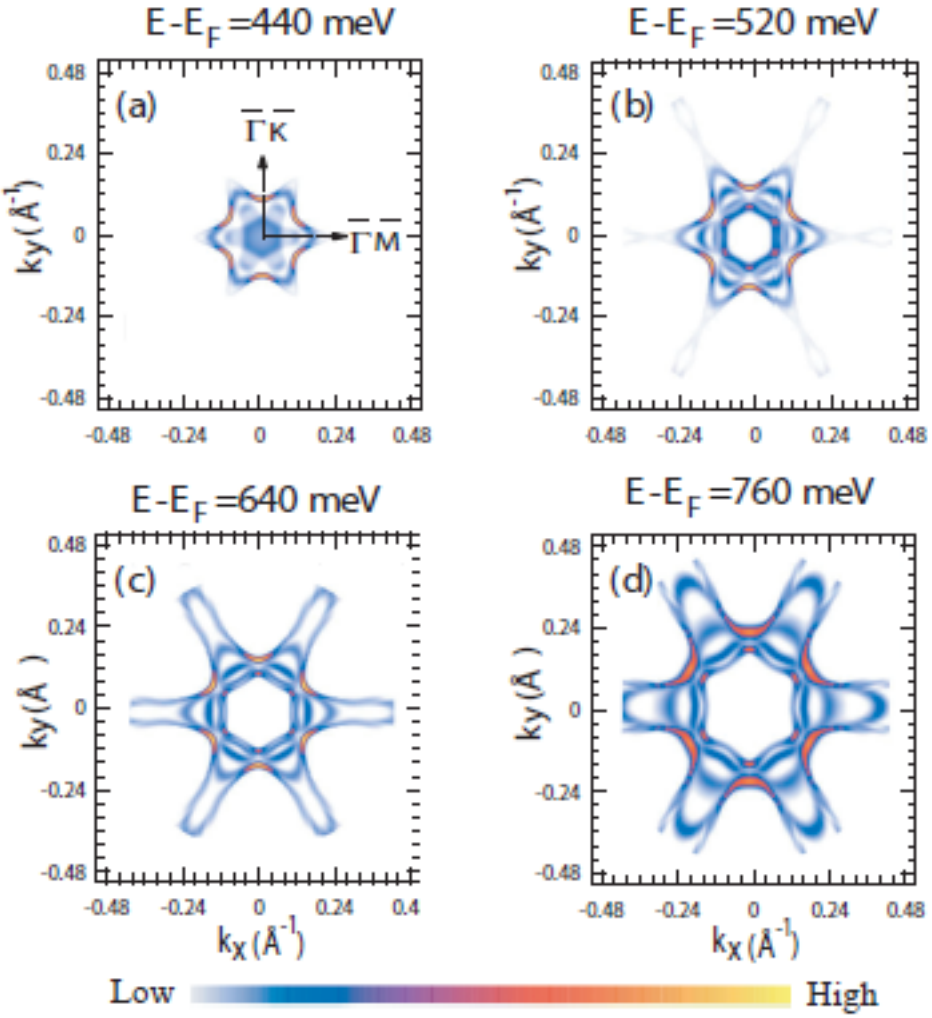

Figure 5.10: (a)–(c) Spatially resolved Fermi surfaces. The color scale shows the constant energy cuts of the surface spectral function $N(E, k_\parallel)$ (Taken from [69]).

The angular distribution of the spin polarization perpendicular to the surface for the two surface states, TSS and ISS, is shown in Figs. 5.11(a)–5.11(d). Here the x, y axis indicate the k_x and k_y, the color (z-axis) shows up-down spin, the spot size indicates the intensity of spin polarization. The net spin density is integrated over a half of the slab, and the net spin is normalized to the electron charge in the integration region. Both surface states are spin polarized and can allow a backscattering between states of parallel momentum and spin component.

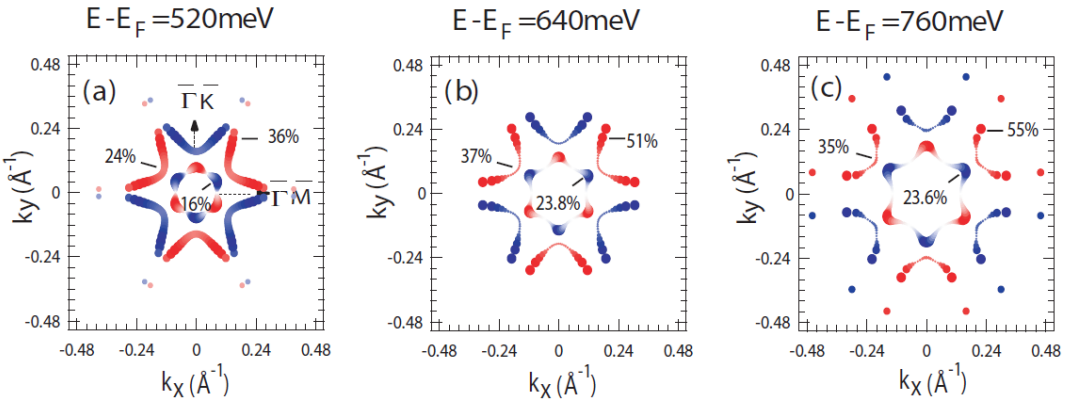

Figure 5.11: (a)–(c) Distribution of the spin polarization perpendicular to the surface, red and blue circles denote positive and negative spin polarization and their sizes represent the magnitudes of spin polarization. The spin polarization values are shown at some specific points (Taken from [69]).

The TSS is somewhat stronger localized than the ISS [cf. Figs. 5.9(b) and 5.9(c)], and it exhibits a higher out-of-plane spin polarization. It is most interesting that the magnitude of the out-of-plane spin polarization of the TSS may be as large as 55%.

Scattering between time reversal partners vanishes as a consequence of time reversal symmetry and dominated by wave vectors accounting for spin polarization. Figure 5.12(a) shows schematic CECs of the TSS. Three characteristic scattering vectors denoted as q_1, q_2, and q_3 explain the features in Fig. 5.12(b). The most intense croissant-shaped features can only be explained by q_2 and $q_2{}'$ which connect two flat segments of the contour as shown in Fig. 5.12(a). Other scattering features along

the $\bar{\Gamma}\bar{M}$ direction characterized by q_1 and q_3, can also be explained as due to the warping of TSS. The scattering originating from ISS can be excluded because it's CEC has no parallel fragments to cause a large joint density of states, and its convex shape does not lead to the croissant-shaped structures.

The intensity maxima of the FFT power profiles in the $\bar{\Gamma}\bar{M}$ direction in Fig. 5.5(a) are plotted and compared with the q values extracted from the slab calculation to quantify the relation between experimental and theoretical results, see Fig. 5.12(c). By shifting the calculated points upward by 0.1 eV we were able to reproduce all the

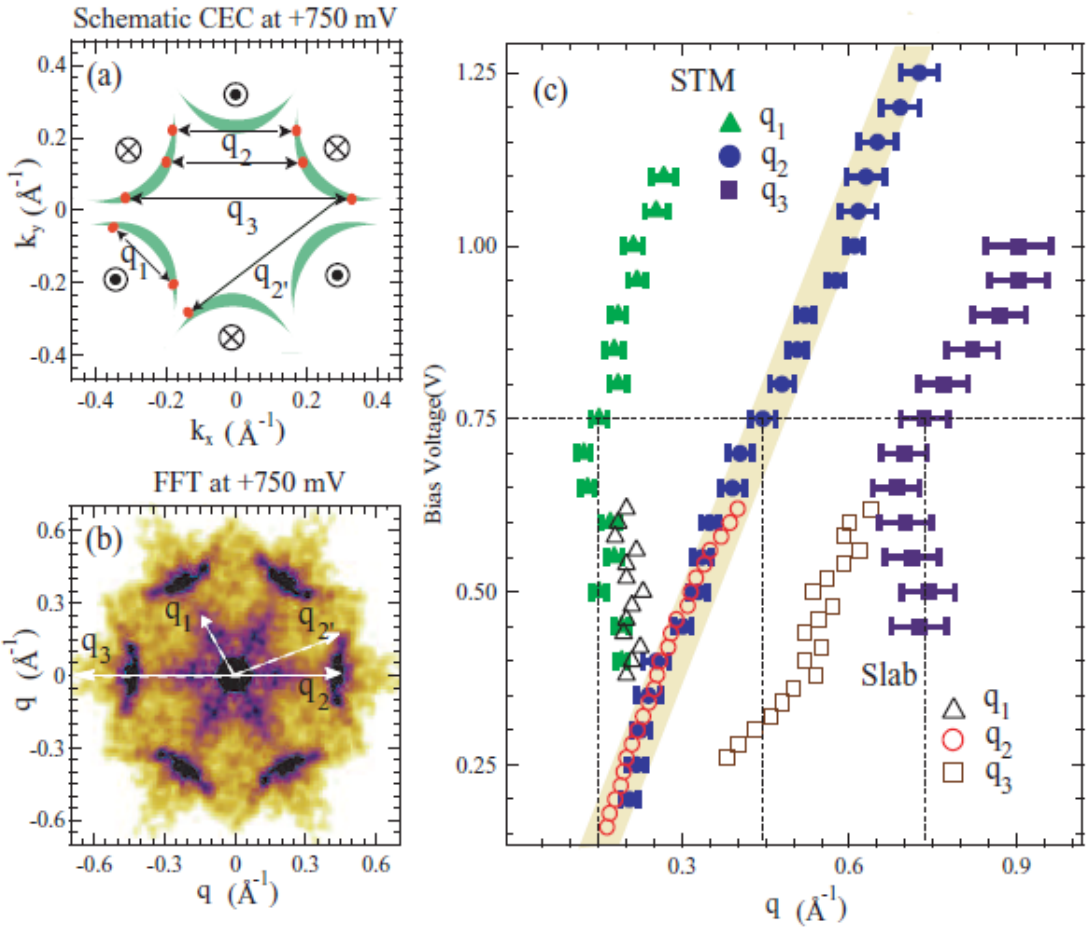

Figure 5.12: (a) Schematic CEC with possible scattering vectors and (b) experimental FFT image at a bias voltage of +750 mV. The $\bar{\Gamma}\bar{M}$ direction is along the x-axis. (c) Dispersion of three scattering vectors from STM (filled symbols) and slab calculation (open symbols) (Taken from [69]).

experimentally observed scattering features. (A discrepancy of the same order between the two photon photoemission measurements of the unoccupied Dirac cone and calculations was reported in Ref. [58].)

The presence of the FFT features in the $\bar{\Gamma}\bar{M}$ direction and their absence in the $\bar{\Gamma}\bar{K}$ direction tells us that the scattering is strongly spin selective. This scattering scenario holds for the whole energy interval from $+300$ to $+1000$ mV above the Fermi energy, and no significant surface to bulk scattering is observed, in contrast to Bi_2Se_3, for which a bulk-related scattering has been reported [74]. This indicates that a coupling of the TSS with the bulk continuum states is negligible even in the unoccupied region, which energetically overlaps with the bulk conduction band.

5.5 Conclusion

Bias voltage dependent scattering of the topological surface state is studied by scanning tunneling microscopy/spectroscopy for a clean surface of the topological insulator Bi_2Te_2Se. A strong warping of constant energy contours in the unoccupied part of the spectrum is found to lead to a spin-selective scattering and further clarified by the $k.p$ model Hamiltonian and *ab initio* calculations. The topological surface state persists to higher energies in the unoccupied range far beyond the Dirac point, where it coexists with the bulk conduction band.

6 Conclusion

In conclusion, our scanning tunneling microscopy/spectroscopy experiment have been performed in combination with the first-principles calculation and $k.p$ model Hamiltonian of Bi_2Te_2Se, one of the most promising three-dimensional topological insulators (3D TIs). Despite quasiparticle interference in 3D topological insulators due to the hexagonal warping effect has been studied for several years, we have unraveled for the first time unoccupied topological surface state of Bi_2Te_2Se with a clear scattering pattern.

The imaged quasiparticle interference pattern on the cleaved surface of Bi_2Te_2Se originates from the strongly warped constant energy contours of the topological surface state with substantial out-of-plane spin polarizations which has been further clarified by the $k.p$ model Hamiltonian and *ab initio* calculations. This is a novel message deduced from new data not available at the time of the previous work.

The clear linear dispersion relation exhibits the linear behavior up to 1000 mV

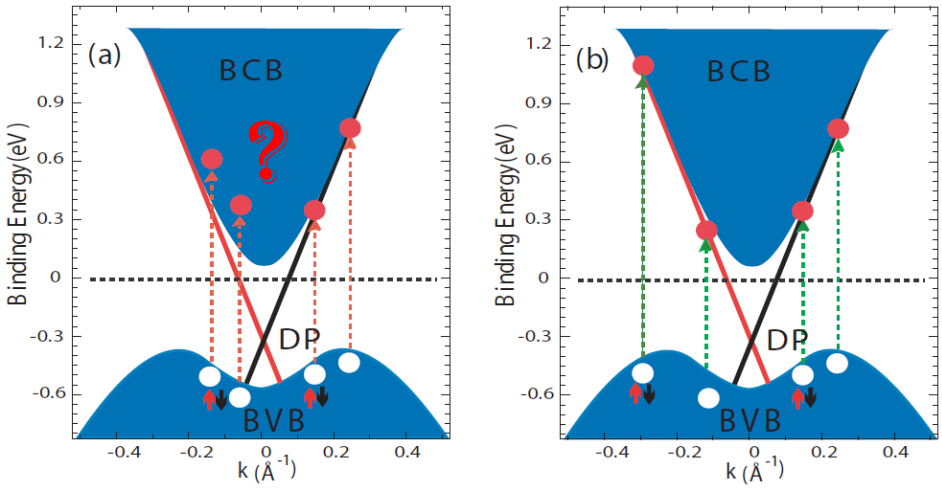

Figure 6.1: (a) Depiction of inter-band optical excitation from bulk valence band to surface state. (b) Depiction of inter-band optical excitation from bulk valence band to surface state after delay time.

related to the Fermi energy, which gives the important information for transport and electronic properties.

The topological surface state is thus found to survive up to energies far above the Dirac point. This finding provides a deeper understanding of optically excited spin and charge dynamics at the surface of topological insulators [see Fig. 6.1] and paves a way to designing opto-spintronic devices.

Bibliography

[1] M.Z. Hasan and C.L. Kane., Colloquium: Topological insulators. *Rev. Mod. Phys*. **82**, 3045 (2010).

[2] J.E. Moore., The birth of topological insulators. *Nature* **464**, 194 (2010).

[3] L. Fu, C.L. Kane, and E.J. Mele., Topological insulators in three dimensions. *Phys.Rev. Lett*. **98**, 106803 (2007).

[4] X.L. Qi and S.C. Zhang., Topological insulators and superconductors. *Rev. Mod. Phys*. **83**, 1057 (2011).

[5] M.Z. Hasan and J.E. Moore, Ann. Review. *Condensed Matter Physics*.**2**, 55-78 (2011).

[6] T. Okuda and A. Kimura, Spin and Angle-resolved photoemission of strong orbit coupled systems. *J. Phys. Soc. Jpn* **82**, 021002 (2013).

[7] J.E. Moore., Topological insulators the next generation. *Nat Phys*.**5**, 378–380 (2009).

[8] X.L. Qi, R. Li, J. Zang, S.C. Zhang., Inducing a magnetic monopole with topological surface states. *Science* **323**,1184–1187 (2009).

[9] P. Hosur., *Phys. Rev. B* **83**, 035309 (2011)

[10] J.A. Sobota, S. Yang, J.G. Analytis, Y.L. Chen, I.R. Fisher, P.S. Kirchmann, and Z.X. Shen., *Phys. Rev.Lett*. **108**, 117403 (2012)

[11] G. Binnig, H. Rohrer, Ch. Gerber, and E. Weibel., Tunneling through a controllable vacuum gap. *Appl. Phys. Lett.* **40**, 178–180 (1982).

[12] G. Binnig, H. Rohrer, Ch. Gerber, and E. Weibel., Surface studies by scanning tunneling microscopy. *Phys. Rev. Lett*. **49**, 57– 61 (1982).

[13] G. Binnig, Rohrer., Scanning tunneling microscopy—from birth to adolescence. *Rev. Mod. Phys*. **59**, 615 (1987).

[14] J.Bardeen., *Phys. Rev. Lett.* **6,** 57(1961).

[15] J. Tersoff and D. R. Hamann. Theory of the scanning tunneling microscope., *Phys. Rev. B* **31**, 805–813, (1985).

[16] C.J. Chen., Introduction to Scanning Tunneling Microscopy. Oxford University Press. 1993.

[17] R. Widmer and R. Fasel, *MNT Vorlesung: Scanning Tunneling Microscopy (STM)* (EMPA, Thun, 2005).

[18] G. Binnig, N. Garcia, H. Rohrer, J. M. Soler, and F. Flores., Electron- metal-surface interaction potential with vacuum tunneling: Observation of the image force. *Phys. Rev. B* **30**, 4816 (1984).

[19] J. M. Pitarke, P. M. Echenique, and F. Flores., Apparent barrier height for tunneling electrons in STM. SURF. SCI. **217**, 267 (1989).

[20] L. Olesen, M. Brandbyge, M. R. Sørensen, K. W. Jacobsen, E. Lægsgaard, I. Stensgaard, and F. Besenbacher., Apparent barrier height in scanning tunneling microscopy revisited. *Phys. Rev. Lett*. **76**, 1485 (1996).

[21] T. W. Michael Schmid., adapted from the IAP/TU Wien STM Gallery, edited by http://www.nationmaster.com/encyclopedia/Image: ScanningTunneling microscope schematic.png, (2005).

[22] O. Fischer, M. Kugler, I. M. Aprile, and C. Berthod., Scanning tunneling spectroscopy of high-temperature superconductors. *Rev. Mod. phys*. **79**, 353 (2007).

[23] M .Cardona and L. Ley. Photoemission in Solids I. *Topics in Applied Physics. **26*** (1978).

[24] S. Hüfner. Photoelectron Spectroscopy: Principles and Applications. *3rd edition.* (Springer, Berlin, (2003).

[25] H. Hertz., Über einen Einfluß des ultravioletten Lichtes auf die electrische Entladung. *Annalen der Physik und Chemie* **31** 983-1000, (1887).

[26] W. Hallwachs., Über den Einfluß des Lichtes auf electrostatisch geladene

Körper. *Annalen der Physik und Chemie* **33** 301-12, (1888).

[27] A. Einstein., Über einen die Erzeugung und Verwandlung des Lichtes betreffenden heuristischen Gesichtspunkt. *Ann. Phys.* **17** 132-48, (1905)

[28] F. Reinert and S. Hüfner., Photoemission spectroscopy—from early days to recent applications. *New Journal of Physics.* **7**, 97 (2005)

[29] A. Kaminski and H. M. Fretwell., On the extraction of the self-energy from angle-resolved photoemission spectroscopy. *New Journal of Physics.* **6**, 98 (2004)

[30] A. Damascelli, Z. Hussain, and Z. Shen, Angle-resolved photoemission studies of the cuprate superconductors, *Rev. Mod. phys*. **75**, 473 (2003).

[31] A. Hiraya, K. Yoshida, S. Yagi, M. Taniguchi, S. Kimura, H. Hama, T. Takayama and D. Amano. *J. Synchrotron Rad*. **5**,445 (1998).

[32] T. Matsui, H. Sato, K. Shimada, M. Arita, S. Senba, H. Yoshida, K. Shirawasa, M. Morita, A. Hiraya, H. Namatame and M. Taniguchi. *Nucl. Instrum. Meth. A* **537**, 467-468 (2001).

[33] P. Hohenberg and W. Kohn., Inhomogeneous Electron Gas. *Phys. Rev. B.* **136**, 864 (1964).

[34] K.V. Klitzing, G. Dorda, and M. Pepper., New method for high-accuracy determination of the fine-structure constant based on quantized hall resistance. *Phys. Rev. Lett*., 45, 494 (1980).

[35] C. L. Kane and E. J. Mele., Z_2 topological order and the quantum spin hall effect. *Phys. Rev. Lett*. **95**, 146802 (2005).

[36] H. M. Guo and M. Franz., Theory of quasiparticle interference on the surface of a strong topological insulator. *Phys. Rev. B*. **81**, 041102 (2010).

[37] J. E. Moore and L. Balents., Topological invariants of time-reversal-invariant band structures. *Phys. Rev. B.* **75**, 121306 (2007).

[38] Rahul Roy., Z_2 classification of quantum spin hall systems: An approach using

time-reversal invariance. *Phys. Rev. B*. **79**, 195321(2009).

[39] M. König, S. Wiedmann, C. Brüne, A. Roth, H. Buhmann, L. W. Molenkamp, X. L. Qi, and S. C. Zhang., Quantum spin hall insulator state in Hg/Te quantum wells. *Science*. **318**, 766, (2007)

[40] A. Roth, C. Brüne, H. Buhmann, L. W. Molenkamp, J. Maciejko, X. L. Qi, and S. C. Zhang., Nonlocal transport in the quantum spin hall state. *Science*, **325**, 294 (2009).

[41] D. Hsieh, D. Qian, L. Wray, Y. Xia, Y. S. Hor, R. J. Cava, and M. Z. Hasan., A topological dirac insulator in a quantum spin hall phase. *Nature*. **452**, (2008).

[42] Y. Xia, D. Qian, D. Hsieh, L. Wray, A. Pal, H. Lin, A. Bansil, D. Grauer, Y. S. Hor, R. J. Cava, and M. Z. Hasan., Observation of a large-gap topological insulator class with a single dirac cone on the surface. *Nature Physics*. **5**, 398 (2009).

[43] Y. L. Chen, J. G. Analytis, J.-H. Chu, Z. K. Liu, S.-K. Mo, X. L. Qi, H. J. Zhang, D. H. Lu, X. Dai, Z. Fang, S. C. Zhang, I. R. Fisher, Z. Hussain, and Z. X. Shen., Experimental realization of a three-dimensional topological insulator Bi_2Te_3. *Science*.**325**,178 (2009).

[44] L. Fu and C. L. Kane., Topological insulators with inversion symmetry. *Phys. Rev. B* **76**, 045302 (2007).

[45] R. E. Prange and S. M. Girvin., The quantum hall effect. *Springer*, New York, 1987.

[46] J. E. Avron, D. Oscadchy, and R. Deiler., a topological look at the quantum hall effect. *PhysicsToday*. 38-42, (2003)

[47] Haldane, F. D. M., Model for a Quantum Hall Effect without Landau Levels: Condensed-Matter Realization of the "Parity Anomaly". *Phys. Rev. Lett*. **61**, 2015 (1988).

[48] S. Murakami., Quantum Spin Hall Effect and Enhanced Magnetic Response by

Spin-Orbit Coupling. *Phys. Rev. Lett*. **97**, 236805 (2006).

[49] Zheng liu et al., Stable Nontrivial Z_2 Topology in Ultrathin Bi (111) Films: A First-Principles Study. *Phys. Rev. Lett*. **107**, 136805 (2011).

[50] D. Hsieh, Y. Xia, D. Qian, L. Wray, F. Meier, J. H. Dil, J. Osterwalder, L. Patthey, A. V. Fedorov, H. Lin, A. Bansil, D. Grauer, Y. S. Hor, R. J. Cava, and M. Z. Hasan., Observation of time-reversal-protected single-dirac-cone topological insulator states in Bi_2Te_3 and Sb_2Te_3. *Phys. Rev. Lett*. **103**,146401 (2009).

[51] K. Kuroda, M. Arita, K. Miyamoto, M. Ye, J. Jiang, A. Kimura, E.E. Krasovskii, E.V. Chulkov, H. Iwasawa, T. Okuda, K. Shimada, Y. Ueda, H. Namatame, and M. Taniguchi., Hexagonally Deformed Fermi Surface of the 3D Topological Insulator Bi_2Se_3. *Phys. Rev Lett.* **105**, 076802 (2010).

[52] N. P. Butch, K. Kirshenbaum, P. Syers, A. B. Sushkov, G. S. Jenkins, H. D. Drew, and J. Paglione., Strong surface scattering in ultrahigh-mobility Bi_2Se_3 topological insulator crystals. *Phys. Rev.B* **81**, 241301(R) (2010).

[53] K. Eto, Z. Ren, A. A. Taskin, K. Segawa, and Y. Ando., Angular-dependent oscillations of the magnetoresistance in Bi2Se3 due to the three-dimensional bulk Fermi surface. *Phys. Rev. B* **81**, 195309 (2010).

[54] Z. Alpichshev, J.G. Analytis, J.H. Chu, I.R. Fisher,Y.L. Chen, Z.X. Shen, A. Fang, and A. Kapitulnik., STM Imaging of Electronic Waves on the Surface of Bi_2Te_3: Topologically Protected Surface States and Hexagonal Warping Effects. *Phys.Rev. Lett*. 104, 016401 (2010).

[55] L.L. Wang, and D.D. Johnson., Ternary tetradymite compounds as topological insulators. *Phys. Rev. B* **83**, 241309(R) (2011).

[56] T. Arakane, T. Sato, S. Souma, K. Kosaka, K. Nakayama, M. Komatsu, T. Takahashi, Z. Ren, K. Segawa, and Y. Ando., Tunable Dirac cone in the topological insulator $Bi_{2-x}Sb_xTe_{3-y}Se_y$. *Nature Comms*. **3**, 636 (2012).

[57] M. Neupane, S. Y. Xu, L. A. Wray, A. Petersen, R. Shankar, N. Alidoust, C. Liu,

A. Fedorov, H. Ji, J. M. Allred, Y.S. Hor, T.R. Chang, H.T. Jeng, H. Lin, A. Bansil, R.J. Cava, and M.Z. Hasan., Topological surface states and Dirac point tuning in ternary topological insulators. *Phys. Rev. B* **85**, 235406 (2012).

[58] D. Niesner, Th. Fauster, S.V. Eremeev, T.V. Men- shchikova, Yu.M. Koroteev, A.P. Protogenov, E.V. Chulkov, O.E. Tereshchenko, K.A. Kokh, O. Alekperov, A. Nadjafov, and N. Mamedov, Unoccupied topological states on bismuth chalcogenides. *Phys. Rev. B*. **86**, 205403 (2012).

[59] K. Miyamoto, A. Kimura, T. Okuda, H. Miyahara, K. Kuroda, H. Namatame, M. Taniguchi, S.V. Eremeev, T.V. Menshchikova, E.V. Chulkov, K.A. Kokh, and O.E. Tereshchenko., Topological Surface States with Persistent High Spin Polarization across the Dirac Point in Bi2Te2Se and Bi2Se2Te. *Phys. Rev. Lett*. **109**, 166802 (2012).

[60] Z. Ren, A.A. Taskin, S. Sasaki, K. Segawa, and Y. Ando, Large bulk resistivity and surface quantum oscillations in the topological insulator Bi_2Te_2Se. *Phys. Rev. B*. **82**, 241306(R) (2010).

[61] J. Xiong, A. C. Petersen, D.X. Qu, R. J. Cava, N. P. Ong., Quantum Oscillations in a Topological Insulator Bi_2Te_2Se with Large Bulk Resistivity. *Phy. E* **44**, 917 (2011)

[62] Omicron NanoTechnology GmbH, 65232 Taunusstein, Germany. 21, 33

[63] C. R. Hammond, The elements, In Handbook of Chemistry and Physics, CRC press, 81st edition, 2004.

[64] I. Ekvall, E. Wahlstr¨om, D. Claesson, H. Olin, and E. Olsson., Preparation and characterization of electrochemically etched W tips for STM. Meas. *Sci. Technol*. **10**, 11 (1999).

[65] V. T. Binh., In situ fabrication and regeneration of microtips for scanning tunneling microscopy. *Journal of Microscopy*, **152**, 355 (1988).

[66] J. P. Ibe, P. P. Bey Jr., S. L. Brandow, R. A. Brizzolara, N. A. Burnham, D. P.

DiLella, K. P. Lee, C. R. K. Marrian, and R. J. Colton., On the electrochemical etching of tips for scannin tunneling microscopy. *Journal of Vacuum Science and Technology* A, **8**, 3570 (1990).

[67] L. Ottaviano, L. Lozzi, and S. Santucci. Scanning Auger microscopy study of W tips for scanning tunneling microscopy. *Review of Scientific Instruments*. 74,3368 (2003).

[68] R. J. Hamers, R. M. Tromp, and J. E. Demuth, Surface Electronic Structure of Si (111)-(7×7) Resolved in Real Space. *Phys. Rev. Lett*. 56, 1972 (1986).

[69] Munisa Nurmamat, E. E. Krasovskii, K. Kuroda, M. Ye, K. Miyamoto, M. Nakatake, T. Okuda, H. Namatame, H. Namatame, M. Taniguchi, E. V. Chulkov, K. A. Kokh, O. E. Tereshchenko, A. Kimura., Unoccupied topological surface state in Bi_2Te_2Se. *Phys. Rev. B*. **88**, 081301(R) (2013).

[70] T. Zhang, P. Cheng, X. Chen, J.F. Jia, X.C. Ma, K. He, L.L. Wang, H.J. Zhang, X. Dai, Z. Fang, X.C. Xie, and Q.K. Xue., Experimental Demonstration of Topological Surface States Protected by Time-Reversal Symmetry. *Phys. Rev. Lett.* **103**, 266803 (2009).

[71] L. Fu., Hexagonal Warping Effects in the Surface States of the Topological Insulator Bi_2Te_3. *Phys. Rev. Lett*. **103**, 266801 (2009).

[72] P. Roushan, J. Seo, C.V. Parker, Y.S. Hor, D. Hsieh, D. Qian, A. Richardella, M.Z. Hasan, R.J. Cava and A. Yazdani., Topological surface states protected from backscattering by chiral spin texture. *Nature* **460**, 1106 (2009).

[73] Z. Alpichshev, J.G. Analytis, J.H. Chu, I.R. Fisher, Y.L. Chen, Z.X. Shen, A. Fang, and A. Kapitulnik., STM Imaging of Electronic Waves on the Surface of Bi_2Te_3 : Topologically Protected Surface States and Hexagonal Warping Effects. *Phys. Rev. Lett*. **104**, 016401 (2010).

[74] S. Kim, M. Ye, K. Kuroda, Y. Yamada, E.E. Krasovskii, E.V. Chulkov, K. Miyamoto, M. Nakatake, T. Okuda, Y. Ueda, K. Shimada, H. Namatame, M.

Taniguchi, and A. Kimura., Surface Scattering via Bulk Continuum States in the 3D Topological Insulator Bi_2Se_3. *Phys. Rev. Lett*. **107**, 056803 (2011).

[75] H. Beidenkopf, P. Roushan, J. Seo, L. Gorman, I. Drozdov, Y.S. Hor, R.J. Cava and A. Yazdani, Spatial fluctuations of helical Dirac fermions on the surface of topological insulators. *Nature* **7**, 939 (2011).

[76] Z. Alpichshev, R.R. Biswas, A.V. Balatsky, J.G. Analytis, J.H. Chu, I.R. Fisher, and A. Kapitulnik, STM Imaging of Impurity Resonances on Bi_2Se_3. *Phys. Rev. Lett*. **108**, 206402 (2012).

[77] M. Ye, S.V. Eremeev, K. Kuroda, E.E. Krasovskii, E.V. Chulkov, Y. Takeda, Y. Saitoh, K. Okamoto, S.Y. Zhu, K. Miyamoto, M. Arita, M. Nakatake, T. Okuda, Y. Ueda, K. Shimada, H. Namatame, M. Taniguchi, and A. Kimura., Quasiparticle interference on the surface of Bi2Se3 induced by cobalt adatom in the absence of ferromagnetic ordering. *Phys. Rev.B*, **85**, 205317 (2012).

[78] Y. Okada, C. Dhital, W.W. Zhou, E.D. Huemiller, H. Lin, S. Basak, A. Bansil, Y.B. Huang, H. Ding, Z. Wang, S.D. Wilson, and V. Madhavan, *Phys. Rev. Lett*. **106**, 206805 (2011).

[79] K.A. Kokh, B.G. Nenashev, A.E. Kokh, and G.Y. Shvedenkov., *J. Crystal Growth*. **275**, e2129 (2005).

[80] S. Jia, H. Beidenkopf, I. Drozdov, M.K. Fuccillo, J. Seo,J. Xiong, N.P. Ong, A. Yazdani, and R.J. Cava., Defects and high bulk resistivities in the Bi-rich tetradymite topological insulator $Bi_{2+x}Te_{2-x}Se$. *Phys. Rev. B*. **86**, 165119 (2012).

[81] Self-consistent calculation within the local density approximation were performed with the full-potential augmented plane wave method described in E.E. Krasovskii, F. Starrost, and W. Schattke., *Phys. Rev. B* **59**, 10504 (1999).

List of publications

1. Unoccupied topological surface state in Bi_2Te_2Se.

   Munisa Nurmamat, E. E. Krasovskii, K. Kuroda, M. Ye, K. Miyamoto, M. Nakatake, T. Okuda, H. Namatame, H. Namatame, M. Taniguchi, E. V. Chulkov, K. A. Kokh, O. E. Tereshchenko, A. Kimura.

   Phys. Rev. B, **88**, 081301(R) (2013).

Other publications

1. Experimental verification of the surface termination in the topological insulator $TlBiSe_2$ using core-level photoelectron spectroscopy and scanning tunneling microscopy.

   Kenta Kuroda, Mao Ye, Eike F. Schwier, Munisa Nurmamat, Kaito Shirai, Masashi Nakatake, Shigenori Ueda, Koji Miyamoto, Taichi Okuda, Hirofumi Namatame, Masaki Taniguchi, Yoshifumi Ueda, Akio Kimura.

   Phys. Rev. **B** 88, 245308 (2013).

Acknowledgement

First and foremost, I wish to thank Prof. Taniguchi and Prof. Galif offer the opportunity to communicate with proficient staff scientists in condensed-matter physics region at Graduate school of science and Hisor of Hiroshima University. I have been very lucky to work on my Ph.D. surrounded by such a large group of talented and kind people. It is an understatement to say that the work presented in this thesis would not have been possible without them. I am not sure their help and contributions can be thanked enough.

I would especially like to thank Prof. Kimura. I feel lucky to have him as my advisor. His deep understanding of physics and exceptional experimental expertise has set a good example of an experimental physicist for me. His enthusiam about Physics, as well as serious work attitude, has created a very productive environment for the group. I am most grateful for his constant reminder to trust in my own abilities and judgment, as well as for his renewed encouragement to risk thinking outside the box and choose challenging yet important research problems.

The work in this thesis is the research I performed at LT-STM and BL-7 of Hisor.
I need to thank Dr. Ye and Dr. Nakatake, from whom learned everything I know about how STM works. I also sincerely wish to thank Dr. Miyamoto for helping me finish the experiment by ARPES part. It is very rare to see anyone like him who knows almost every aspect of photoemission experiments.

I really need to acknowledge all the help I have gotten from theorists, Prof. Krasovskii and Prof. Chulkov who worked at DIPC, they gave a great effort to explain our experimental results. I have been very lucky to get such high quality sample from Prof. Tereshchenko's group, it make smooth our experiment.

I have benefitted a lot from various professional and personal interactions with my

fellow physics students and friends in our group, Mr. Kuroda, Dr. Utsumi, Mr. Zhu, Dr. Jiang and Dr. Nakashima — thank you! A special thanks goes to Mr. Kuroda again, who has been of particular help in many ways. It has been an honor and a privilege to share the highs and lows of graduate school with him. Thank you for always finding time to help despite your busy schedules.

Finally, thanks to my parents for all their support and good wishes. They have encouraged me nearly every day of my entire life and helped me through so many problems and challenges.